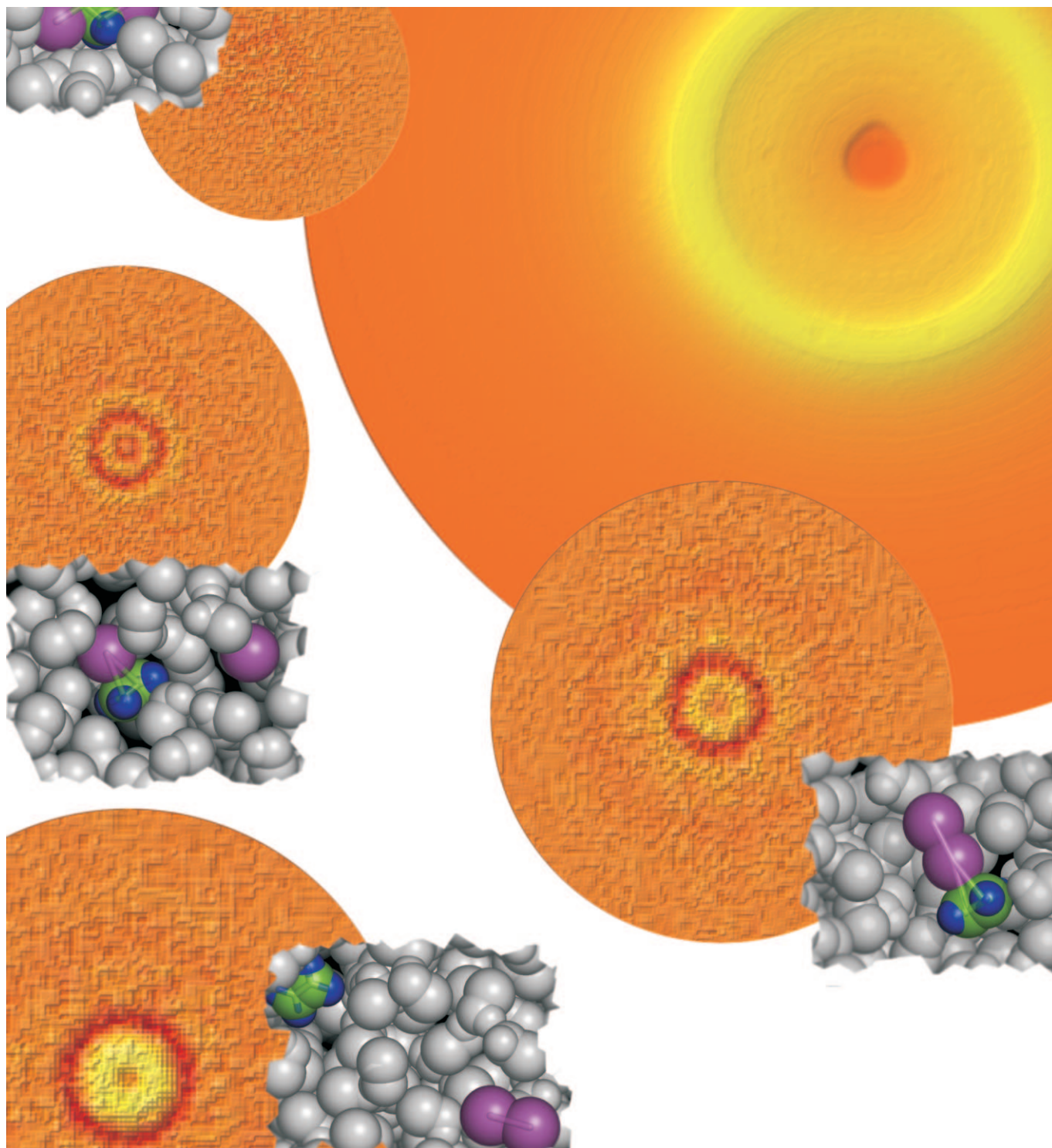


Spatiotemporal Kinetics in Solution Studied by Time-Resolved X-Ray Liquidography (Solution Scattering)

Tae Kyu Kim,^[b] Jae Hyuk Lee,^[a] Michael Wulff,^[c] Qingyu Kong,^[d] and Hyotcherl Ihee^{*[a]}



Information about temporally varying molecular structure during chemical processes is crucial for understanding the mechanism and function of a chemical reaction. Using ultra-short optical pulses to trigger a reaction in solution and using time-resolved X-ray diffraction (scattering) to interrogate the structural changes in the molecules, time-resolved X-ray liquidography (TRXL) is a direct tool for probing structural dynamics for chemical reactions in solution. TRXL can provide direct structural information that is difficult to extract from ultrafast optical spectroscopy, such as the time dependence of bond lengths and angles of all molecular species including short-lived intermediates over a wide range of times, from picoseconds to milliseconds. TRXL elegantly complements ultrafast optical spectroscopy because the diffraction signals are sensitive to all chemical species simultaneously and the diffraction signal from each chemical species can be quantitatively calcu-

lated from its three-dimensional atomic coordinates and compared with experimental TRXL data. Since X-rays scatter from all the atoms in the solution sample, solutes as well as the solvent, the analysis of TRXL data can provide the temporal behavior of the solvent as well as the structural progression of all the solute molecules in all the reaction pathways, thus providing a global picture of the reactions and accurate branching ratios between multiple reaction pathways. The arrangement of the solvent around the solute molecule can also be extracted. This review summarizes recent developments in TRXL, including technical innovations in synchrotron beamlines and theoretical analysis of TRXL data, as well as several examples from simple molecules to an organometallic complex, nanoparticles, and proteins in solution. Future potential applications of TRXL in femtosecond studies and biologically relevant molecules are also briefly mentioned.

1. Introduction

Diffraction is the most common and accurate method for determining molecular structure on the atomic length scale. Using diffraction methods with modern sources and detection techniques, impressive progress has been made in unraveling highly complex structures including biomolecules. For example, most three-dimensional structures of proteins have been determined by X-ray crystallography, where diffraction from a well-ordered protein single crystal is measured. Usually the structures determined by diffraction methods represent the averaged structure of the most stable configurations in equilibrium, but by adopting the pump-probe scheme commonly used for time-resolved optical spectroscopy,^[1–9] even transient structures occurring in the course of a chemical reaction can be obtained.^[10–37] In this scheme, a reaction in the molecules is initiated by an optical pulse (pump), and the time evolution of the induced structural changes is probed, at a given delay, by the diffraction of a short X-ray or electron pulse that replaces the optical probe pulse in time-resolved optical spectroscopy.

Time-resolved structural studies have been established by using electron^[10–24] and X-ray diffraction techniques.^[25–35] Since electrons and X-rays interact with matter quite differently, these two methods are highly complementary. Due to the nearly million-fold higher scattering cross section for electrons than for X-rays, time-resolved electron diffraction has been applied to the transient structural studies of dilute or thin samples, such as molecules in the gas phase,^[11–13,15,16] surfaces,^[10,17,18] nanostructures,^[19–22] and thin films.^[23,24] In contrast, X-ray pulses are capable of revealing transient structures of bulk samples, such as crystals and liquids with a thickness in the 10–100 μm range. Femtosecond X-ray sources, such as a laser-driven plasma^[38] and an accelerator-based source,^[39,40] have been used to investigate the dynamics of acoustic phonons, heating, nonthermal behavior near the melting point, and phase transitions in simple crystalline samples with ~ 100 fs temporal resolution. In such cases, the system under study is quite simple which means that the structural dynamics

can be probed by monitoring one or a few Bragg spots with time. To follow the atomic positions of all the atoms in more complex systems, almost all Bragg diffraction spots need to be recorded as a function of time, and thus the current femtosecond X-ray sources cannot be used due to their insufficient photon flux. Instead, high-brilliance synchrotron sources have been used to study transient structural changes in small organic,^[41,42] inorganic,^[43,44] and complex protein molecules.^[45–47] In crystals. For example, the conformation changes of proteins during their biological function have been tracked, in single crystals, by time-resolved Laue crystallography with 100 ps time resolution.^[45–47]

All the samples mentioned so far are either single crystals or in polycrystalline form. During the last decade it has been demonstrated that the transient structures can be captured even in liquid samples by using the same time-resolved diffraction (scattering) method. To distinguish the applications for liquid samples from other studies on crystalline samples, we propose to call it time-resolved X-ray liquidography (TRXL).^[25–35] TRXL is a technique that can be used to unravel intermediate structures and their spatiotemporal kinetics in the solution phase where most reactions relevant to chemical synthesis, bi-

-
- [a] J. H. Lee, Prof. H. Ihee
Center for Time-Resolved Diffraction, Department of Chemistry
Graduate School of Nanoscience & Technology (WCU), KAIST
Daejeon 305-701 (Republic of Korea)
Fax: (+82) 42-350-2810
E-mail: hyotcherl.ihee@kaist.ac.kr
- [b] Prof. T. K. Kim
Department of Chemistry and Institute of Functional Materials
Pusan National University, Busan 609-735 (Republic of Korea)
- [c] Prof. M. Wulff
European Synchrotron Radiation Facility
6 Rue Jules Horowitz, BP 220, 38043 Grenoble Cedex (France)
- [d] Dr. Q. Kong
Société Civile Synchrotron SOLEIL, L'Orme des Merisiers
Saint-Aubin BP 48, 91192 Gif-sur-Yvette Cedex (France)

ology, and industrial applications occur. For studying the structural dynamics of molecules in solution, time-resolved X-ray absorption spectroscopy^[48–50] serves as a complementary tool. A brief comparison of TRXL and time-resolved X-ray absorption spectroscopy will be given below along with a comparison of TRXL and time-resolved optical spectroscopy.

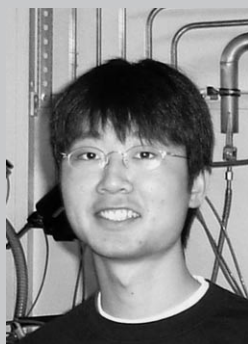
In the solution phase, the solute species (molecules, ions, or atoms of interest) are dissolved in a solvent that in most cases

outnumbers the solute. Since X-rays scatter and diffract from all atom–atom pairs, the signal has three principal contributions: i) the solute-only term from the internal structure of the solute molecules, ii) the solvent-only term from the bulk solvent, and iii) the solute–solvent cross term from solute–solvent atomic pairs. In general, the solvent-only term dominates the others. For this reason, diffraction is not the most sensitive tool to elucidate the structure of a solute. In addition, the information about the structural changes is contained in the difference in the diffraction intensity measured with and without excitation. Typically only a fraction of the solute species is excited by the optical excitation. Therefore, the laser-induced change in the diffraction signal (difference diffraction intensity) is embedded in a strong background signal from the solvent. Upon photoexcitation, the solutes absorb photons and might undergo various reaction pathways, which affects the solute-only and the solute–solvent cross terms. The absorbed photon energy is eventually transferred to the solvent, thereby changing the thermodynamic state of the solvent, that is, its temperature, pressure, and density. Therefore, the solvent-only term also changes with time.^[25,26] In summary, the TRXL signal is extremely weak with a low signal-to-noise ratio, but at the same time it contains rich information about the structural changes of not only the solute but also the solvent. The analysis of

Tae Kyu Kim, born in 1976 in South Korea, received his B.S. and M.S. degrees in chemistry at KAIST and his PhD in physical chemistry at KAIST in 2004, investigating photodissociation dynamics of small molecules and clusters. Afterwards he worked with Prof. Hyotcherl Ihee as a postdoctoral fellow in KAIST and focused on the structural dynamics of small molecules in solution using time-resolved X-ray liquidography. He is currently an assistant professor at Pusan National University (Korea). He has lately, in collaboration with Bob Schoenlein at the ALS, used ultrafast X-ray absorption spectroscopy on photochemically interesting molecules in solution.



Jae Hyuk Lee was born in 1983 in South Korea, and received his B.S. degree in chemistry at KAIST, South Korea. He is a PhD candidate under the supervision of Prof. Hyotcherl Ihee at KAIST. He is investigating the structural dynamics of various molecular systems ranging from small molecules to proteins in the solution phase using ultrafast X-ray liquidography.



Michael Wulff received a Masters Degree in mathematics and physics from the Niels Bohr Institute, University of Copenhagen, in 1981 and a PhD in solid-state physics from the Cavendish Laboratory, University of Cambridge, in 1985. He then joined Gerry Lander at the Transuranium Institute in Karlsruhe (1985–1989) where he worked on the magnetic structure of actinides using neutron scattering. He joined the European Synchrotron Radiation Facility (ESRF) in 1990 as responsible for the Laue beamline ID09. He received the M. T. Meyer Award from the University of Cambridge in 1984. In 2001 he received the Röntgen Medal from the University of Wurzburg. In 2003 he was appointed Adjoin Professor at the Niels Bohr Institute and in the Chemistry Department at the University of Copenhagen.



Qingyu Kong, born in 1972 in China, received B.S. and M.S. degrees in optical and laser physics at Shandong University in 1998 and a PhD in physical chemistry at Fudan University, Shanghai, in 2001, on the formation and photofragmentation reactions of metallofullerenes. Starting as a postdoctoral fellow as a beamline scientist from 2003 to 2007, he worked with Michael Wulff in ESRF, and focused on time-resolved X-ray scattering on small molecules in solution. From 2007 to the present, he is beamline scientist at the Soleil Synchrotron near Paris, studying catalytic chemistry and lithium-ion batteries with time-resolved dispersive EXAFS.



Hyotcherl Ihee obtained a B.S. from KAIST and a PhD from Caltech in 2001 under the supervision of Prof. Ahmed Zewail, developing ultrafast electron diffraction. He then joined Prof. Keith Moffat at the University of Chicago as a postdoctoral fellow working on protein structural dynamics using time-resolved X-ray crystallography. In 2003, he became a faculty member at KAIST where he continues to contribute to the advancement of TRXL. His current research interests focus on molecular structural dynamics probed by time-resolved electron/X-ray diffraction and spectroscopy.



TRXL data requires accurate theoretical modeling, which involves quantum calculations, molecular dynamics (MD) simulations, and global-fitting analysis. We have recently revealed the structural reaction dynamics of several interesting molecules in solution by TRXL, with innovations in synchrotron and beam-line technology and developments in data analysis.^[25–35]

This review focuses on the experimental technique, the data analysis, and examples of how TRXL reveals structural dynamics and kinetics in solution. The enormous advances in time-resolved X-ray diffraction from crystalline materials and surfaces^[36] and in time-resolved X-ray absorption spectroscopy in condensed systems^[48–50] are not the subjects of this article. The review is organized as follows. In Section 2, the basic experimental and theoretical concepts of TRXL are discussed. This is followed by a review of recent TRXL studies with emphasis on photochemistry in the solution phase (Section 3). The application examples include simple molecules, organometallic complexes, nanoparticles, and protein molecules in solution. Finally, the perspectives of extending TRXL to femtosecond studies and biologically relevant molecules are briefly presented.

2. Experiment and Analysis of TRXL

2.1. Basic Principle of Liquid X-ray Diffraction and Scattering

The general theory of X-ray diffraction from a disordered sample is well established.^[51–53] This section summarizes the basic formulas used in structure determination from TRXL data. X-ray diffraction from a disordered sample is often called diffuse scattering to distinguish it from the diffraction from well-ordered crystalline planes (Bragg diffraction). The system under consideration is a spatially isotropic liquid. When scattering and diffraction from an optically excited system is considered, the system might not be isotropic just after the excitation due to the possible polarization of the exciting light.

However, since the X-ray pulse length in our synchrotron diffraction studies is rather long (~100 ps) compared with the rotation time of small molecules in solution (~10 ps), we can approximate the system to be isotropic. In addition, the rather long X-ray pulse length allows us to treat the system as being in quasi-equilibrium during the exposure, although the structures might change over longer times. The X-ray diffraction intensity is typically expressed as a function of \mathbf{q} , the momentum transfer between the incident (\mathbf{k}_0) and the elastically scattered (\mathbf{k}) X-ray waves (see Figure 1). The magnitude of \mathbf{q} is a

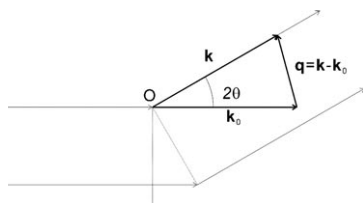


Figure 1. Schematic representation of the scattering geometry: the relationship between the incoming X-ray (\mathbf{k}_0), the scattered X-ray (\mathbf{k}), and momentum transfer vector \mathbf{q} .

function of the X-ray wavelength and the scattering angle 2θ between \mathbf{k} and \mathbf{k}_0 as shown in Equation (1):

$$q = \frac{4\pi}{\lambda} \sin \theta \quad (1)$$

The basic expression for the amplitude of the diffracted electric field, neglecting multiple scattering, is given by Equation (2):

$$A(\mathbf{q}) = \int \rho_e(\mathbf{r}) \exp(-i\mathbf{q} \cdot \mathbf{r}) d\mathbf{r} \quad (2)$$

where $\rho_e(\mathbf{r})$ is the electron density of the sample. Since we are interested in the atomic positions \mathbf{r}_n , we express the total electron density in the sample as a superposition of electron densities centered on the atomic positions [Eq. (3)]:

$$\rho_e(\mathbf{r}) = \sum_n \rho_n(\mathbf{r} - \mathbf{r}_n) \quad (3)$$

where ρ_n is the electron density of the n th atom and \mathbf{r} is a certain position from the origin. The combination of Equations (2) and (3) leads to the new expression [Eq. (4)]:

$$\begin{aligned} A(\mathbf{q}) &= \int \sum_n \rho_n(\mathbf{r} - \mathbf{r}_n) \exp(-i\mathbf{q} \cdot \mathbf{r}) d\mathbf{r} \\ &= \sum_n \exp(-i\mathbf{q} \cdot \mathbf{r}_n) \int \rho_n(\mathbf{r} - \mathbf{r}_n) \exp(-i\mathbf{q} \cdot (\mathbf{r} - \mathbf{r}_n)) d(\mathbf{r} - \mathbf{r}_n) \\ &= \sum_n f_n(\mathbf{q}) \exp(-i\mathbf{q} \cdot \mathbf{r}_n) \end{aligned} \quad (4)$$

with a new function, $f_n(\mathbf{q})$, for the scattering from the n th atom (the so-called atomic form factor), which is the Fourier transform of the electron density of atom n [Eq. (5)]:

$$f_n(\mathbf{q}) = \int \rho_n(\mathbf{r}) \exp(-i\mathbf{q} \cdot \mathbf{r}) d\mathbf{r} \quad (5)$$

Since the atom can be approximated as a spherical object, $f_n(\mathbf{q})$ depends only on the modulus of \mathbf{q} , that is, $f_n(q)$. Usually the atomic form factor for a specific atom can be approximated by the following expression [Eq. (6)]:

$$f(q) = \sum_{i=1}^4 a_i \exp(-b_i(q/4\pi)^2) + c \quad (6)$$

where the parameters a_i , b_i , and c are tabulated Cromer–Mann parameters.^[54] In fact Equation (6) is an angularly averaged form of Equation (5). Since the scattering intensity is the square modulus of the scattering amplitude, the scattered intensity, $S^{\text{elastic}}(\mathbf{q})$ of elastic scattering can be described by Equation (7):

$$S^{\text{elastic}}(\mathbf{q}) = \left| \sum_n f_n(\mathbf{q}) \exp(-i\mathbf{q} \cdot \mathbf{r}_n) \right|^2 \quad (7)$$

$$= \sum_n \sum_m f_n(\mathbf{q}) f_m(\mathbf{q}) \exp(-i\mathbf{q} \cdot (\mathbf{r}_n - \mathbf{r}_m))$$

where indexes m and n include all atoms in the sample. In noncrystalline materials such as liquids and gases, the molecules are randomly oriented. The symbol S is used for scattering intensity and should not be confused with entropy. The isotropic averaging of Equation (7) leads to the Debye Equation [Eq. (8)]:

$$S^{\text{elastic}}(q) = \left\langle \sum_n \sum_m f_n(\mathbf{q}) f_m(\mathbf{q}) \exp(-i\mathbf{q} \cdot (\mathbf{r}_n - \mathbf{r}_m)) \right\rangle_{\Omega}$$

$$= \sum_n \sum_m f_n(\mathbf{q}) f_m(\mathbf{q}) (1/4\pi) \int_0^{\pi} \exp(-iqr_{nm} \cos \alpha) 2\pi \sin \alpha \, d\alpha$$

$$= \sum_n \sum_m f_n(\mathbf{q}) f_m(\mathbf{q}) \frac{\sin qr_{nm}}{qr_{nm}}$$

$$= \sum_n f_n^2(\mathbf{q}) + \sum_n \sum_{m \neq n} f_n(\mathbf{q}) f_m(\mathbf{q}) \frac{\sin qr_{nm}}{qr_{nm}} \quad (8)$$

Here, r_{nm} is the distance between the n th and m th atoms. In reality, this expression is not convenient to use for the liquid phase because of the large number of possible combinations of n and m . Instead, if $\rho_{ij}(r)$ is defined as the density of the i -type atom around the j -type atom at a distance r , there are $4\pi r^2 \rho_{ij}(r) dr$ of the j -type atoms in the distance range r to $r + dr$ from an i -type atom, and Equation (8) becomes [Eq. (9)]:

$$S(q) = \sum_i N_i f_i^2(\mathbf{q}) + \sum_i \sum_{i \neq j} N_i f_i(\mathbf{q}) f_j(\mathbf{q}) \int_V 4\pi r^2 \rho_{ij}(r) \frac{\sin qr}{qr} dr \quad (9)$$

where the indexes i and j now run over the different atom types and N_i is the number of i -type atoms. This is a more general expression of the scattered intensity for an amorphous sample. As the distance r increases, the density ρ_{ij} converges to the average density (ρ_0) of the j -type atom in the sample. The scattered intensity from this average atom density is completely negligible except at small scattering angles, often not accessible in the experiment because it is too close to the primary (non scattered) X-ray beam. Accordingly the scattering intensity at small angles can be subtracted from Equation (9) on the basis that it is negligible in the range of observable angles. In this case, the scattering intensity of the third term of Equation (10a) is negligible and can be expressed by Equation (10b):

$$S(q) = \sum_i N_i f_i^2(\mathbf{q}) + \sum_i \sum_{i \neq j} N_i f_i(\mathbf{q}) f_j(\mathbf{q}) \int_V 4\pi r^2 (\rho_{ij}(r) - \rho_{0j}) \frac{\sin qr}{qr} dr$$

$$+ \sum_i \sum_{i \neq j} N_i f_i(\mathbf{q}) f_j(\mathbf{q}) \int_V 4\pi r^2 \rho_{0j} \frac{\sin qr}{qr} dr \quad (10a)$$

$$S(q) = \sum_i N_i f_i^2(\mathbf{q}) + \sum_i \sum_{i \neq j} N_i N_j f_i(\mathbf{q}) f_j(\mathbf{q}) \int_V 4\pi r^2 \rho_0 (g_{ij}(r) - 1) \frac{\sin qr}{qr} dr \quad (10b)$$

where $g_{ij}(r)$ is the pair distribution function between atom types i and j . The radial distribution function (RDF) is defined such that $4\pi r^2 g_{ij}(r) dr$ is the probability of finding a j -type atom at the distance r from an i -type atom. Equations (8) and (10) are important in the theoretical modeling of experimental TRXL data. The difference diffraction signal in TRXL measurements has three contributions as explained in Section 1. Likewise one can separate the RDF [$g_{ij}(r)$ in Eq. (10)] into three different contributions as shown in Figure 2. The first contribu-

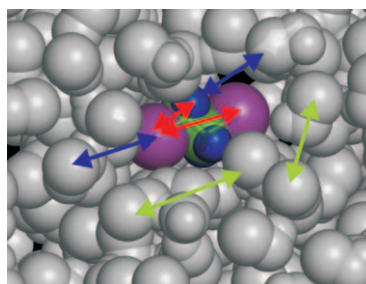


Figure 2. Schematic representation of the three principal $g_{ij}(r)$ contributions for the $C_2H_4I_2$ molecule dissolved in methanol. The C, H, and I atoms are colored in green, blue, and purple, respectively. The solvent is shown in gray. Red arrows indicate interatomic pairs for the solute only and the blue and green arrows represent solute-solvent and solvent-only pairs, respectively.

tion is the $g_{ij}(r)$ of the solute. In this case i and j represent the atoms within the molecule and $g_{ij}(r)$ describes its (internal) structure. The $g_{ij}(r)$ functions are usually very sharp at interatomic distances (typically 2–5 Å for small molecules, but can be longer for larger molecules). Correlations between different solutes are usually negligible in diluted solutions. For example, for CHI_3 dissolved in CH_3OH ^[32] at a concentration of 20 mM, the average distance between CHI_3 molecules is ~27 Å. The second contribution is the $g_{ij}(r)$ of the solvent. This term describes the structure of bulk solvent and thus is dependent on the thermodynamic variables, that is, temperature, pressure, and density. The third contribution is the $g_{ij}(r)$ for the solute-solvent cross term. This represents the structure of the solvent around the solutes. An example of $g_{ij}(r)$ and the corresponding scattering intensity $S(q)$ is shown in Figure 3 for I_2 dissolved in CCl_4 .

The structural dynamics information is contained in the change in the scattered intensity as a function of time, $\Delta S(q,t)$.

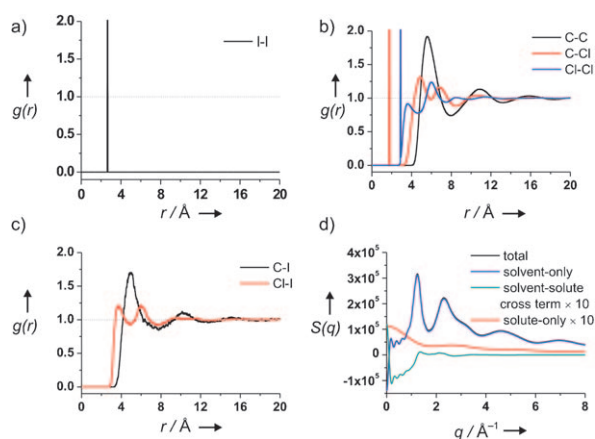


Figure 3. $g_{ij}(r)$ for the atom–atom pairs for I_2 in CCl_4 . a) $g_{ij}(r)$ for I_2 (solute-only term); b) $g_{ij}(r)$ for the solvent pairs C–C, C–Cl, and Cl–Cl in CCl_4 (solvent-only term); and c) $g_{ij}(r)$ for the solute–solvent cross term. The $g_{ij}(r)$ values are calculated in equilibrium by MD simulation for one I_2 molecule in 256 CCl_4 molecules. d) Scattering intensity for each contribution calculated with the $g_{ij}(r)$ values by using Equation (10). The solvent scattering (blue line) is the sum of $S(q)$ curves from C–C and Cl–Cl pairs, and the solute–solvent cross term (dark cyan) is the sum of the $S(q)$ curves for the I–C and I–Cl pairs. The solute-only scattering intensity (red) is calculated from the $g_{ij}(r)$ of I–I. The intensities of the solute–solvent cross term and the solute-only term are multiplied by 10 to enhance their visibility. Because the ratio of solute to solvent molecules is extremely small, the scattering intensity from the solvent dominates the total scattering.

Since the scattered signal is proportional to Z^2 (Z =atomic number), solute molecules with heavy atoms increase the relative ratio of the solute-related terms, $\Delta S_{\text{solute-only}}(q,t)$ and $\Delta S_{\text{solute-solvent}}(q,t)$, against the solvent-only term $\Delta S_{\text{solvent-only}}(q,t)$. Figure 4a compares the solvent-only and solute-only terms for the photodissociation of Cl_2 and I_2 in CCl_4 . The solute-only term is comparable to the solvent-only term for I_2 in CCl_4 , but it is much smaller for Cl_2 in CCl_4 .

Although the scattered intensity probes all structures in the solution mixture, a more intuitive real-space interpretation is obtained by sine-Fourier transforming $qS(q)$ into a radial density $S(r)$ [Eq. (11 a,b)]:

$$S(r) = \frac{1}{2\pi^2 r} \int_0^\infty qS(q) \sin(qr) dq = \frac{C}{V} \left\{ \sum_{i \neq j} w_{ij} [g_{ij}(r) - 1] \right\} \quad (11a)$$

$$w_{ij}(r) = \int_0^\infty dq f_i(q) f_j(q) \cos(qr) \quad (11b)$$

where C is a constant, the w_{ij} are weighting coefficients, and V is the volume of the system. By defining $S(r)$ in this way one can obtain information on the average $g_{ij}(r)$ weighted by the X-ray form factors.

So far we have described the elastic scattering, which contains the average molecular structure of the solution. However, X-ray photons also scatter inelastically with the scattered X-rays having slightly longer wavelengths. Since inelastically scattered waves do not interfere, the inelastic scattering is independent of structure; it depends only on the number and type

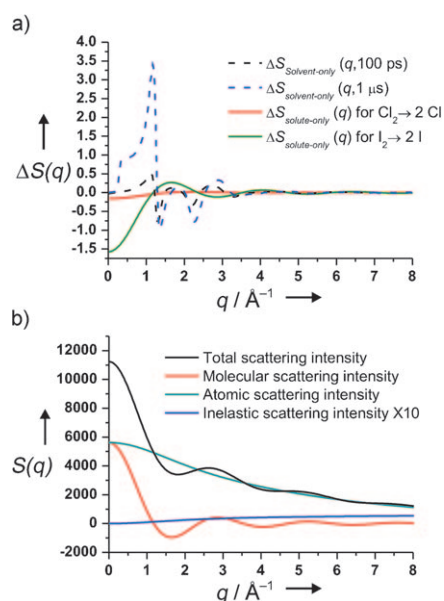


Figure 4. a) Comparison of $\Delta S_{\text{solvent-only}}(q)$ and $\Delta S_{\text{solute-only}}(q)$ curves for the photolysis of Cl_2 and I_2 in CCl_4 . Typical $\Delta S_{\text{solvent-only}}(q)$ curves at 100 ps and 1 μ s are shown in black and blue broken lines, respectively. $\Delta S_{\text{solute-only}}(q)$ curves for the photolysis of Cl_2 and I_2 in CCl_4 are shown as red and green solid lines, respectively. b) Intensities for I_2 in the gas phase. The black curve is the sum of elastic and inelastic scattering. The blue curve is the inelastic scattering multiplied by 10. The green curve is $2f^2(q)$ for an iodine atom, the first (self) term in Equation (8), and the red curve is the second (interference) term in Equation (8).

of atoms in a molecule. The inelastic scattering intensity can be calculated with Equations (12) and (13):

$$S_{\text{inelastic}}(q) = \left[Z - \frac{S_{\text{elastic}}(q)}{Z} \right] \times \{ 1 - M[\exp(-Kq/4\pi) - \exp(-Lq/4\pi)] \} \quad (12)$$

$$S_{\text{inelastic}}(q) = Z \left[\frac{a}{(1 + bq/4\pi)^c} \right] \quad (13)$$

where Z in Equation (12)^[55] is the atomic number, and K , L , and M are atomic constants. Equation (13)^[56] is for heavier atoms, from Ca to Am. The inelastic intensity increases with q (Figure 4b). The inelastic intensity does not change during the reaction because it does not depend on structure and the fact that the mass of the involved atoms is conserved. It is useful to include the inelastic scattering term for finding the absolute scattering from the sample. For the sake of comparison, the elastic and inelastic intensities for I_2 in the gas phase are shown in Figure 4b. The magnitude of the inelastic intensity is much smaller than that of the elastic scattering intensity at lower q , but as q increases, the inelastic scattering intensity increases while the elastic scattering intensity decreases.

2.2. TRXL Experiments

In a time-resolved X-ray experiment, we need to initiate a given reaction and then open the X-ray shutter and record the X-ray scattering as a function of time. Unfortunately the time resolution of large-area charge-coupled device (CCD) detectors, which are essential for capturing a large fraction of the scattered beam, is milliseconds at best. This time resolution is significantly longer than the ultrafast timescales in chemical reactions. The pump-probe method is therefore used to improve the time resolution at the cost of lowering the data collection efficiency. The sample is excited by a short laser pulse and the structure of the sample is probed by a delayed X-ray pulse, as in time-resolved laser spectroscopy. With the advent of third-generation synchrotrons, pulsed hard X-ray pulses with a pulse length of ~ 100 ps are now available and can be used for time-resolved experiments. However, the time separation of X-ray pulses from a synchrotron ranges from a few nanoseconds to hundreds of nanoseconds, which is significantly shorter than the readout time of a conventional area detector. To reach the ultimate time resolution limited by the X-ray pulse length itself, it is necessary to isolate a single pulse from the adjacent pulses with a mechanical chopper. Since the chopper greatly decreases the flux of the X-ray photons (ph s^{-1}), the polychromatic beam from a narrow-bandwidth undulator is often used in solution experiments where the q resolution can be relaxed to increase the signal-to-noise ratio. These approaches have been implemented on beamline ID09B at the European Synchrotron Radiation Facility (ESRF) and the subsection below describes this in more detail. Figure 5a shows the TRXL scheme. It comprises a closed capillary jet (or an open-liquid jet) that supplies a fresh sample for every laser/X-ray pulse pair, a short-pulse laser, a high-speed chopper that selects single X-ray pulses, and an integrating area detector.

2.2.1. Laser-Excitation and X-ray-Probe Scheme

In a typical TRXL experiment, an ultrashort (100 fs–2 ps) optical laser pulse initiates a photochemical process in a molecule of interest in the solution phase, and a 100 ps X-ray pulse from a synchrotron is sent to the volume to probe the structural dynamics. The X-ray diffraction patterns are measured as a function of the time delay between the excitation laser pulse (pump) and the X-ray pulse (probe). The time resolution is determined by several factors, such as the temporal durations of pump and probe pulses and the timing jitter between two pulses.

2.2.2. Pulsed X-rays from the Synchrotron

Most TRXL measurements have been performed on beamline ID09B at the ESRF, which is dedicated to a variety of pump-probe experiments.^[26,28–33,35] The ESRF, which was inaugurated in 1994, is a third-generation synchrotron and is specifically designed to produce very intense, collimated beams of hard X-rays between 5 and 100 keV (0.1–2.5 Å). The electrons in the storage ring are accelerated to 6.03 GeV in the 844-m-long

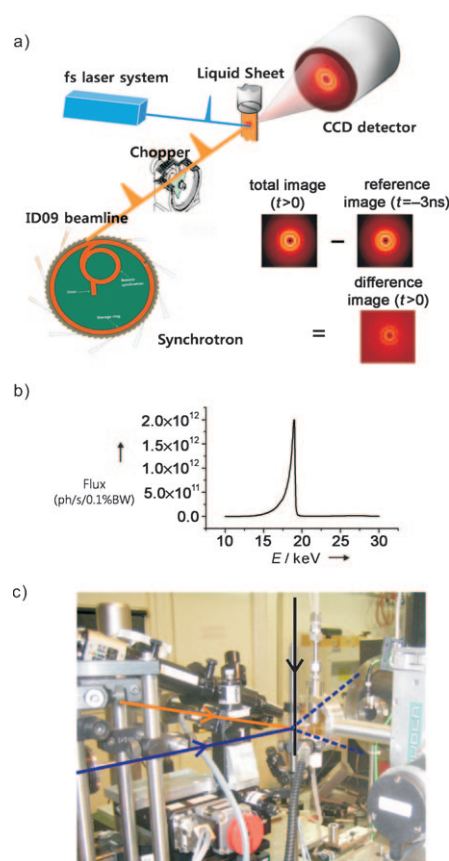


Figure 5. a) Experimental setup for a TRXL experiment. X-rays from a synchrotron are guided through a beamline and selected by a high-speed mechanical X-ray chopper. The chopper consists of a flat triangular disk spinning at the same frequency as the laser. The laser pulses excite the sample and the time-delayed X-ray pulses probe the photoinduced structural changes as diffraction images on the CCD detector. The difference diffraction image for a given positive time delay is generated by subtracting the reference image at -3 ns from the diffraction image. b) Spectral shape of an X-ray pulse generated by the U17 undulator. To increase the signal-to-noise ratio the raw quasi-monochromatic (3% bandwidth) X-ray beam is used. c) Picture of the TRXL setup on ID09B. The blue and orange lines represent the paths of the X-ray and laser beams, respectively. Both beams are overlapped in the most stable region of the jet (300 μm thickness). Diffraction patterns from the scattered X-rays are recorded by a MarCCD detector.

storage ring. Synchrotron sources typically deliver 50–150 ps X-ray pulses of polychromatic radiation. At ESRF, the electron bunches rotate around the storage ring in 2.82 μs , which corresponds to an X-ray frequency of 355.4 kHz. In uniform filling mode, the electrons are evenly spaced and separated by 2.84 ns. This filling mode is not suitable for TRXL because it is impossible to select single pulses with a mechanical chopper from such a densely filled pulse train. The solution is to use filling patterns with fewer bunches, such as the one-bunch, four-bunch, 16-bunch, or hybrid mode. The 16-bunch mode is well suited for TRXL liquid experiments in which 16 electron bunches (90 mA) are evenly spaced by 176 ns. The bunch length is about 100 ps (full width at half maximum, FWHM) and a single pulse can be isolated by the high-speed chopper on beamline ID09B.

The X-ray pulses are generated by a 236-pole in-vacuum undulator with a magnetic period of 17 mm (U17) with magnets inside the vacuum vessel of the storage ring. The undulator spectrum can be shifted in energy by varying the distance between the undulator magnets, the undulator gap, from 15 keV at the closed gap position at 6 mm to 20.3 keV at the open gap position at 30 mm. At a 9 mm gap, the undulator spectrum is dominated by its first harmonics, which peaks at ~ 18.0 keV ($\lambda = 0.67$ Å) with a $\sim 3\%$ bandwidth. This quasi-monochromatic beam is used to increase the flux and hence shortens the exposure time by a factor of 250 over strictly monochromatic experiments with silicon crystals (Figure 6b). The X-ray beam is focused by a platinum-coated toroidal mirror into a spot size of 0.1×0.06 mm². Each X-ray pulse delivers $\sim 10^9$ X-ray photons to the sample and its duration varies from 90 to 150 ps depending on the bunch charge in the fill pattern. The frequency of the X-ray pulses from a 16-bunch fill is 5.7 MHz, that is, much faster than a normal amplified femtosecond laser that typically operates around 1 kHz. Since laser and X-ray pulses have to arrive on the sample in pairs, the frequency of the X-ray has to be lowered to that of the laser, which is accomplished by a high-speed chopper (Julich). The mechanical chopper is a flat triangular disk that is spinning at the frequency of the laser. One of edges of the triangular rotor has a shallow channel that terminates with small roofs. The channel is thus a semi-open tunnel with slits at the ends. When the

tunnel is parallel to the direction of the beam, the single X-ray pulse is selected. The short (225 ns) opening window and the low rotation jitter (3–4 ns) ensure the selection of single pulses from the 16-bunch mode (176 ns pulse separation) at 1 kHz.

2.2.3. Laser System

High-intensity laser pulses are needed to excite a significant fraction of the sample. The laser pulse length has to be shorter than or similar to the X-ray pulse length to keep the time resolution as high as possible. For most experiments, we use a Ti-sapphire-amplified femtosecond laser system producing ~ 100 fs pulses at 780 nm with a pulse energy of ~ 2.5 mJ at a repetition rate of 986.3 Hz in phase with the mechanical chopper. By frequency doubling and tripling in a beta barium borate (BBO) crystal, we typically obtain 800 and 250 $\mu\text{J pulse}^{-1}$ at 390 and 260 nm, respectively. Typically the laser pulse is temporally stretched to 2 ps by passing it through fused-silica prisms to prevent multiphoton excitation in the sample. The laser beam is focused to a spot size of 0.12×0.12 mm² with a 10° angle with the X-ray beam. Great care is taken to remove inhomogeneities in the beam profile through the use of spatial filters.

A pump-probe experiment relies on the reproducibility of the time delay between pump and probe pulses. Therefore, the laser pulse has to be accurately synchronized to the X-ray pulse. As described in the previous section, the mechanical chopper isolates a subtrain of pulses at 986.3 Hz, the 360th subharmonic of the radio-frequency (RF) clock. A phase shifter generates the delayed RF clock, which is synchronized with the repetition rates of the laser oscillator (88.05 MHz) and the amplifier (986.3 Hz). The amplified laser pulse is in phase with the chopper. The time delay between the laser and X-ray pulses is controlled electronically by shifting the phase of the oscillator feedback loop with a delay generator with 10 ps resolution. Longer delays (> 10 ns) are realized by amplifying a different seed pulse of the oscillator pulse train. In this way the time delay between the laser and X-ray pulses can be varied by changing the arrival time of the laser pulse. The jitter between the laser and X-ray pulses is less than 5 ps (rms) as measured by a fast GaAs detector (see the following section).

2.2.4. Spatial and Temporal Overlaps

To increase the signal-to-noise ratio of the TRXL data and to define the accurate time delay, the laser and X-ray pulses have to be overlapped at the sample, in space and time. To check the temporal overlap, a fast GaAs detector is placed at the sample position and the laser and X-ray pulses are recorded in one time trace. With a 6 GHz oscilloscope, the relative timing can be adjusted within a few picoseconds by moving the laser firing time. During an experiment, the relative timing between the laser and X-ray pulses is monitored simultaneously and nonintrusively by using fast photodiodes.

The spatial overlap between X-ray and laser pulses is obtained by replacing the sample with a 25- μm -diameter laser pinhole. This allows for checking the laser-X-ray overlap and

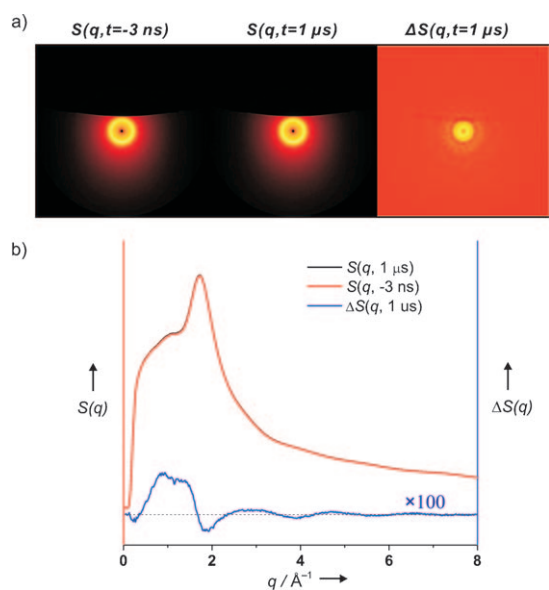


Figure 6. Raw diffraction patterns and curves for CH_3I in methanol recorded by the MarCCD detector. a) Left: raw diffraction image at -3 ns used as a reference for the unperturbed sample; middle: raw diffraction image at $1 \mu\text{s}$; right: difference diffraction image at $1 \mu\text{s}$ after radial integration. The shadow in the upper part of each image is from the nozzle, and can be eliminated by using a better nozzle. b) Radial integrated diffraction intensity curves $[S(q)]$ at $1 \mu\text{s}$ (black, barely visible) and -3 ns (red). The two curves nearly coincide with each other. The difference intensity $[\Delta S(q)]$ at $1 \mu\text{s}$ time delay (blue) is obtained by subtracting the normalized $S(q)$ at -3 ns from the normalized $S(q)$ at $1 \mu\text{s}$. The total intensity curves are normalized to 1 in the range $45^\circ \leq 2\theta \leq 55^\circ$, which forces the curves to cross zero in this range. $\Delta S(q)$ is typically 1000 times weaker than $S(q)$. The $\Delta S(q)$ curve is multiplied by 100 for clarity.

for scanning the laser-beam profile. The pinhole is centered on the X-ray beam and then the laser spot is moved across the center of the pinhole by scanning the position of the focusing lens. For centering the spatial overlap more precisely, the change in the scattering caused by thermal expansion is used, which in a liquid and with the present beam sizes appears after 1 μs . Specifically, we scan the ratio of the scattered intensity between the inner and outer disks of the solvent peak. When the sample has expanded after typically 1 μs , the liquid peak will shift to lower scattering angles. The low-angle scattering increases and the high-angle scattering decreases. Therefore, the ratio between the inner and outer parts of the solvent peak changes in proportion to the laser excitation. The X-ray beam is typically 60 μm vertically and 100 μm horizontally. The laser spot is circular in shape with a diameter of 100–200 μm .

2.2.5. Data Acquisition

The scattered X-ray signals are recorded on a 133-mm-diameter MarCCD detector (recently upgraded to the ESRF/Frelon CCD camera; here we report the MarCCD parameters), which is placed \sim 45 mm downstream of the sample. This allows scattering angles (2θ) from 3 to 60° to be covered. The scattered X-rays are converted into visible light on a phosphor screen in the camera and the image is transferred onto the CCD chips via a fiber-optic taper with a demagnification of 2.7. Scattering images are recorded on a square CCD (2048 \times 2048 pixels) with an effective pixel size of 64.276 μm . The quantum efficiency at 18.0 keV is \sim 50% and the gain in the conversion of X-ray to CCD counts is 1 arbitrary digital unit (ADU) per 18.0 keV X-ray photon. The CCD chip is cooled to -70°C to reduce the dark current to about 0.02 ADU s^{-1} . The readout noise is 0.1 ADU pixel^{-1} . The typical exposure time is less than 5 s, and typically 5×10^9 X-ray photons per image are recorded by the CCD detector. The data acquisition protocol is worked out to minimize the effect of slow drifts in the beam positions, in the detector and in the sample (heating, radiation damage). Diffraction data are typically collected for more than ten time delays spanning from -100 ps to 3 μs , and each time delay is interleaved by a measurement at -3 ns which serves as a reference for the unperturbed sample. Each time sequence is typically repeated more than ten times to make it easier to discriminate bad measurements.

2.2.6. Sample System

Two different sample-cell systems have been used: a dilute solution (0.5–100 mM) or a pure solvent is circulated through either a capillary or an open-jet sapphire nozzle to provide a stable sheet of flowing liquid with a thickness of \sim 0.3 mm. Likewise the diameter in the capillary system is 0.3 mm. In the open-jet nozzle the solution is passed between two flat sapphire crystals with a spacing of 0.3 mm (Kyburz), which makes a stable liquid sheet that is directly exposed to the laser/X-ray beams. The open-jet system has the advantage that the scattering from the capillary is eliminated, which reduces the back-

ground substantially, especially in low-Z liquids such as water. In addition, the capillary is often pierced by the laser beam or the flow is reduced due to deposits inside the capillary. The liquid jet is circulated with a speed of \sim 3 m s^{-1} , fast enough to separate the laser-heated portions of the flowing solution in the 986.3 Hz laser pulse train. The solution from the jet is collected and recycled by passing it through a reservoir.

2.3. Analysis of TRXL Data

2.3.1. Data Reduction—Difference Diffraction Curves

In this section, we describe the data-reduction routines used to generate difference diffraction curves at a specific time delay. The two-dimensional diffraction patterns on the CCD are circularly integrated into one-dimensional diffraction curves [$S(q,t)$] as a function of the momentum transfer q and the time delay t . During this process the effect of the X-ray beam polarization and the effective phosphor-screen thickness (as a function of the scattering angle) is removed. The major difficulty in the data reduction is that the total diffraction intensity contains contributions not only from the solute but also from the solvent, air, and so on.

Figure 6 shows that time-resolved differences are small and therefore care has to be taken before subtraction. In particular, small (0.01%) variations of the scattered intensity can mask the effect of the laser excitation. Since the best I_0 detector for X-ray intensity on ID09B is reliable “only” to about 3×10^{-4} , this type of detector cannot be used for normalization purposes. Instead, the intensities of the total diffraction curves are normalized to 1 at high 2θ angles, in the range from 45 to 55°, which makes the difference diffraction curve cross zero in this range. The assumption is that the signal from any structural change in the solute will oscillate several times around zero in that wide interval, thus ensuring that the curve integral is zero. In addition, the diffraction curve is less sensitive to the changes in solute structure in this 2θ range because the magnitude of the interference oscillation from interatomic distances is greatly damped, that is, atomic scattering dominates in this region. After normalization, the diffraction curve for the unperturbed sample is subtracted from the curve at a positive time delay to generate the difference diffraction curve [$\Delta S(q,t)$]. Then the difference diffraction curve can be put on an absolute scale, defined by the scattering from one solvent molecule, by scaling it to the nonexcited solvent/solute background (including both elastic and inelastic contributions). To convert the difference intensity in absolute electron units per solvent molecule, the raw scattering intensities are compared with the theoretical intensity from one solvent molecule simulated by MD. Once the scattering intensity from a MD simulation is scaled to one solvent molecule, experimental raw scattering intensities can be compared with the theoretical model. Experimental difference curves are further scaled down by normalization factors. In summary, we need to consider the ratio between experimental raw data and theoretical curves, as well as the normalization factor. As shown in Figure 6, the changes

in diffraction intensity are generally much smaller (less than 0.1%) than the total diffraction signal.

To magnify the intensity at high angles (where the signal from the solute-only term dominates the total difference signal), $\Delta S(q,t)$ is multiplied by q (Figure 7). The $q\Delta S(q,t)$ curves

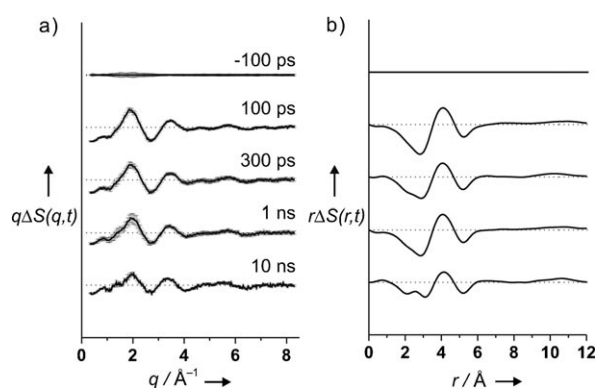


Figure 7. TRXL signals from photodissociation of $C_2F_4I_2$ in methanol at selected time delays (100 ps, 300 ps, 1 ns, and 10 ns). a) Difference intensity $q\Delta S(q)$. Error bars represent the experimental error associated with each scattering angle. b) Difference RDF $r\Delta S(r)$, the sine-Fourier transform of the curves in (a).

amplify the high-resolution part, that is, changes in atom-atom correlations inside molecules, and that function enters directly when calculating the Fourier transform. As expected, the -100 ps curve shows no difference intensity and the difference features only start to appear at positive time delays. It is more intuitive to consider the sine-Fourier transforms, $r\Delta S(r,t)$, of $q\Delta S(q,t)$, where r is the interatomic distance. This real-space representation is a measure of the change in the radial electron density for all atom-atom pairs. Positive and negative peaks mean the formation and depletion of the specific interatomic distance, respectively. The relation between $q\Delta S(q,t)$ and $r\Delta S(r,t)$ is [Eq. (14)]:

$$r\Delta S(r,t) = \frac{1}{2\pi^2} \int_0^\infty q\Delta S(q,t) \sin(qr) e^{-q^2\alpha} dq \quad (14)$$

where α is a damping constant (typically $\alpha=0.03 \text{ \AA}^2$) for the reduction of truncation error caused by the finite accessible q range ($0.5\text{--}8.5 \text{ \AA}^{-1}$) in the TRXL experiment.

Experimental $q\Delta S(q,t)$ and $r\Delta S(r,t)$ curves from the photodissociation of 1,2-diiodotetrafluoroethane ($C_2F_4I_2$) dissolved in methanol^[33] are shown in Figure 7. Because the high- Z I atoms in the solute scatter X-rays more strongly than the low- Z atoms (C, H, and O) in the solvent, the signal from the solute stands out in the $r\Delta S(r,t)$ representation. For example, the negative peak at $\sim 5.0 \text{ \AA}$ corresponds to the initial I-I distance in the parent molecule. However, structure determination in solution from TRXL data requires quantitative analysis of three contributions that are mutually connected by energy conservation in the X-ray-illuminated volume. In the following sections, we describe the theoretical analysis with the global-fitting approach.

2.3.2. Data Analysis—Getting Scattering Components

For the global-fitting analysis in which theoretical difference curves are fitted against the experimental data at all time delays rather than one time delay at a time, the scattering components for the solute-related terms and the solvent-only term need to be estimated theoretically. In fact these components are usually time-independent, which reflects the fact that most molecular transitions are ultrafast whereas their population dynamics are slower. To calculate the scattering intensities $S_k(q)$ for all putative species during a chemical reaction, we use the relationship between the RDFs $g_{ij}(r)$ and $S(q)$ [Eq. (10)]. The $g_{ij}(r)$ for all atomic pairs in the solute-only and solute-solvent cross terms can be calculated by MD simulations with putative solute structures from quantum chemical calculations. More specifically, geometry optimization and energy minimization of the solutes, their candidate intermediates, and their final photoproducts in a solvent environment are calculated by density functional theory (DFT) using the code Gaussian 03.^[57] To describe the solvent environment, the integral-equation-formalism polarizable continuum model (IEFPCM)^[58] is used. These quantum chemical calculations provide optimized geometries and minimized energies for all putative chemical species. Using optimized geometries, MD simulations for all the putative species are performed. We use the MD program MOLDFY,^[59] which gives the $g_{ij}(r)$ functions of all atomic pairs. MD simulations are performed in the (constant) NVT ensemble. Typically the simulation includes one solute molecule and hundreds of solvent molecules (range from 256 to 2048 molecules), and the solute molecule is initially placed in the center of a virtual solvent box. As mentioned above, the internal structure of each molecule is fixed; however, the intermolecular interaction is governed by Coulomb forces and Lennard-Jones potentials. Consequently, from the MD-simulated $g_{ij}(r)$ for a given solute in the solution, the associated X-ray intensity is then derived from [Eq. (15)]:

$$S(q) = \sum_{ij} f_i(q)f_j(q) \left(N_i\delta_{ij} + \frac{N_iN_j}{V} \int_0^\infty (g_{ij}(r) - 1) \frac{\sin(qr)}{qr} 4\pi r^2 dr \right) \quad (15)$$

where $f_i(q)$ is the atomic form factor of the i -type atom, N_i is the number of i -type atoms, δ_{ij} is the Kronecker delta, and V is the volume of the box. This equation is basically the same as Equation (10).

Using Equation (15), one can now calculate the intensity for all putative solutes. The $g_{ij}(r)$ from atomic pairs within the solute, the solute-only term, gives the intensity from a gas of independent molecules, which is calculated by the Debye formula in Equation (8). The solute-solvent cross terms can be calculated by using the $g_{ij}(r)$ for solute-solvent pairs. In this way, one can calculate the scattering components from all putative solutes including their cage structures in the solvent.

We also need to understand the hydrodynamics of solvents after energy transfer from solutes to the solvent. Initially (< 1 ns) the transferred energy heats the solvent and the temper-

ature and pressure build up at constant volume and density.^[26,35] This process can be described by a solvent-specific differential, $(\partial S(q,t)/\partial T)_{\rho}$, which is hereafter referred to as $(\partial S/\partial T)$. The scattering changes due to this term are mainly ascribed to the broadening of atom–atom distances in the solvent, constrained to a constant volume, by adiabatic heating at early times. Then, thermal expansion sets in and the solvent eventually returns to ambient pressure in typically 100 ns at a slightly elevated volume and temperature. Assuming local thermal equilibrium in the solvent, the change in the solvent scattering, at a given time delay t , can be factorized as [Eq. (16)]:

$$\Delta S_{\text{solvent}}(q,t) = \Delta T(t) \left(\frac{\partial S}{\partial T} \right)_{\rho} + \Delta \rho(t) \left(\frac{\partial S}{\partial \rho} \right)_{T} \quad (16)$$

The two differentials $[(\partial S/\partial T)_{\rho}]$ and $(\partial S/\partial \rho)_{T}$ can be obtained in two ways: through MD simulations and a solvent-heating experiment. In the first case, MD simulations are performed as a function of the thermodynamic variables ρ and T . In the simulations for methanol, for example, two temperatures ($T_1=300$ and $T_2=328$ K) and densities ($\rho_1=785.9$ and $\rho_2=759.8$ kg m⁻³) are used. The densities are chosen such that the system is at the same pressure at (T_1, ρ_1) and (T_2, ρ_2) . Three MD simulations are run under the different thermodynamic conditions (T_1, ρ_1) , (T_2, ρ_1) , and (T_2, ρ_2) . Then by taking the difference between the scattering in (T_1, ρ_1) from that in (T_2, ρ_1) and dividing by the temperature difference $(T_2 - T_1)$, the temperature differential at constant density $[(\partial S/\partial T)_{\rho}]$ is obtained. In the same way, subtracting the scattering intensity of the system in (T_2, ρ_2) from that in (T_2, ρ_1) and dividing by the density change $(\rho_1 - \rho_2)$ provides the density differential at constant temperature $[(\partial S/\partial \rho)_{T}]$. The solvent differentials can also be obtained in a separate experiment in which the pure solvent is vibrationally excited, without inducing any structural change, with near-infrared light.^[26] The experimental solvent differentials usually produce better fits in the global analysis since they probe the real solvent response with the pink X-ray spectrum that is also used in the solute experiment. It should be noted that all calculated scattering components need to be corrected for slight polychromaticity of the X-ray beam, that is, the asymmetric 3% bandwidth.

2.3.3. Data Analysis—Global-Fitting Analysis

In this section, we explain the global-fitting analysis^[14,28] which fits the experimental data $[q\Delta S_{\text{exp}}(q,t)]$ at all time delays instead of fitting the data at each time delay separately. In fact all $q\Delta S(q,t)$ curves at all time delays are linked together through the reaction kinetics due to total energy conservation. Global-fitting parameters generally include the rate constants for all reactions, the fraction of excited molecules, the branching ratios among excited molecules, and the size of the laser spot at the sample. In some cases, the geometrical parameters (bond lengths and angles) and the energies of all putative species can also be included in the fitting. The first step is to generate the theoretical difference diffraction curves $q\Delta S_{\text{the}}(q,t)$. As explained, $q\Delta S_{\text{exp}}(q,t)$ has three components (solute-only, solute–

solvent cross, and solvent-only terms) and $q\Delta S_{\text{the}}(q,t)$ can be expressed by [Eq. (17)]:

$$\begin{aligned} \Delta S_{\text{the}}(q,t) &= \Delta S_{\text{solute only}}(q,t) + \Delta S_{\text{solute-solvent}}(q,t) + \Delta S_{\text{solvent only}}(q,t) \\ &= \frac{1}{R} \left[\underbrace{\sum_k c_k(t) S_k(q) - S_g(q) \sum_k c_k(0)}_{\text{solute-only term + solute-solvent cross term}} \right] + \underbrace{\left(\frac{\partial S}{\partial T} \right)_{\rho} \Delta T(t) + \left(\frac{\partial S}{\partial \rho} \right)_{T} \Delta \rho(t)}_{\text{solvent-only term}} \end{aligned} \quad (17)$$

where R is the ratio of solvent to solute molecules, k represents the chemical species (reactant, intermediates, and products), $c_k(t)$ is the fraction of k species after the time delay t , $S_k(q)$ is the scattering intensity of species k , $(\partial S/\partial T)_{\rho}$ is the scattering change with respect to the temperature rise in the solvent at constant density (temperature differential), $(\partial S/\partial \rho)_{T}$ is the scattering response with respect to a change in solvent density at constant temperature (density differential), and $\Delta T(t)$ and $\Delta \rho(t)$ are the changes of the solvent temperature and density at time delay t , respectively. Equation (17) assumes that the diffraction changes from solute transitions are mathematically locked to the solvent response by energy conservation in the X-ray-probed volume.

To be more explicit we will now discuss a very simple reaction [Eq. (18)]:



where R is the ground state, R^* is the state populated just after excitation, I is an intermediate, and P is the final product. Because the structure of the solute changes, this gives the changes in the diffraction intensity in the solute-only term. Also, the transformed solutes adopt new cage structures. Finally, the energy absorbed by the solute is transferred to the solvent and this causes a change in temperature, pressure, and density as a function of time. The structural displacements between the solvent molecules are very small (typically milli-Å), but given their large number, the signal from the temperature and density changes is often comparable to the solute-related terms. Consequently we can connect the solute-related terms and solvent-only term by using the energy conservation provided that we can calculate the energies of all species during the reaction. The underlying ideas are shown in Figure 8.

Once the time-independent intensities $(S_k(q))$, $(\partial S/\partial T)_{\rho}$ and $(\partial S/\partial \rho)_{T}$ are determined, each experimental curve can be used to find the best theoretical curve by using $c_k(t)$, $\Delta T(t)$, and $\Delta \rho(t)$ as fitting parameters. This approach has too many parameters and the fits are unstable. To reduce the number of free parameters we use a global approach, in which theoretical difference curves are fitted at all time delays rather than one time delay at a time. This consists in writing a system of differential equations for the population of species and the energy in solution. Solving rate equations yields the theoretical $c_k(t)$ and $Q(t)$ (heat into the solvent). $\Delta T(t)$, and $\Delta \rho(t)$ are also obtained from $Q(t)$ by solving the hydrodynamics equations. Using this approach, the parameters that control the kinetics are the fitting parameters. For the model reaction of $R \rightarrow R^* \rightarrow$

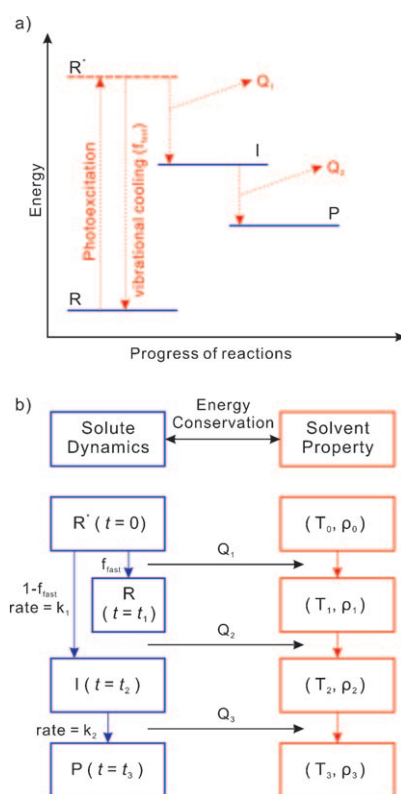


Figure 8. a) Energy transfer from photon-absorbing molecules (R) to the solvent. The ground state of the reactant R is laser-excited to the short-lived state R^* that decays, via vibrational cooling, to R and/or through a reactive pathway to the intermediate (I) and product (P) at times t_2 and t_3 , respectively. The energy difference between the two species transfers to the surrounding solvent molecules. b) Time-dependent solute dynamics and solvent hydrodynamics properties (temperature and density) are linked by energy conservation. Once the energy is transferred from the solute to the solvent, the temperature and density of the solvent change as a function of time. The fraction of excited molecules that return directly to the ground state in a few picoseconds is denoted by f_{fast} .

$I \rightarrow P$, one can set the following rate equations [Eq. (19)]:

$$\begin{aligned} \frac{\delta[R^*]}{\delta t} &= -k_1[R^*] \\ \frac{\delta[I]}{\delta t} &= k_1[R^*] - k[I] \\ \frac{\delta[P]}{\delta t} &= k_2[I] \end{aligned} \quad (19)$$

where k_1 and k_2 are rate constants for the $R^* \rightarrow I$ and $I \rightarrow P$ reactions, respectively. Numerical integration of the rate equations gives an estimation of the fraction of each species [$c_k(t)$] to the total concentration as a function of time. From the estimated $c_k(t)$ and the energies E_k (J molecule⁻¹) from the DFT calculations, the heat transfer $Q(t)$ to the solvent is calculated as a function of time by using Equation (20):

$$\begin{aligned} Q(t) &= \text{Energy}(t=0) - \text{Energy}(t) \\ &= \frac{N_A}{R} \left[\sum_k (E_g + h\nu) c_k(0) - \sum_k E_k c_k(t) \right] \\ &\quad + \frac{N_A}{R} f_{\text{fast}} [1 - \exp(-t/k_{\text{fast}})] \end{aligned} \quad (20)$$

where N_A is Avogadro's number, R is the ratio of the number of solvent molecules per solute, E_g (J molecule⁻¹) is the absolute energy of the parent (ground-state) molecule, $h\nu$ is the excitation energy, and E_k (J molecule⁻¹) is the energy of species k . The symbol f_{fast} denotes the fraction of rapid relaxed species, and k_{fast} (s⁻¹) is the rate constant for vibrational cooling which occurs faster than the temporal resolution of TRXL (~100 ps). $Q(t)$ can be used to calculate the change in temperature [$\Delta T(t)$] and density [$\Delta \rho(t)$] as a function of time through the following hydrodynamics relations (Livak equation, Eq. (21)):^[60]

$$\begin{aligned} \Delta P(t) &= \frac{\alpha_p}{\chi_T C_V} \int_{-\infty}^t \frac{\partial Q}{\partial t'}(t') \exp(-((v_s/a)(t-T'))^2) dt' \\ \Delta T(t) &= \frac{Q(t) - (C_V - C_P) \frac{\chi_T}{\alpha_p} \Delta P(t)}{C_P} \\ \Delta \rho(t) &= \rho_0 [\chi_T \Delta P(t) - \alpha_p \Delta T(t)] \end{aligned} \quad (21)$$

where C_V (J mol⁻¹ K) and C_P (J mol⁻¹ K) are the heat capacity at constant volume and constant pressure, respectively, χ_T is the isothermal compression constant, α_p is the isobaric dilatation constant, ρ_0 is the density of the solvent, a is the radius of the laser spot, and v_s is the speed of sound in the solvent. Using the estimated values of $c_k(t)$, $\Delta T(t)$, and $\Delta \rho(t)$, one has $\Delta S_{\text{the}}(q,t)$ at all time delays from Equation (17). A least-squares fitting using the chi-squared value between $\Delta S_{\text{the}}(q,t)$ and $\Delta S_{\text{exp}}(q,t)$ is the final step in the global-fitting analysis. The definition of chi squared (χ^2) used is [Eq. (22)]:

$$\begin{aligned} \chi^2 &= \sum_t \chi_t^2 \\ &= \sum_t \sum_q \left(\frac{(\Delta S_{\text{the}}(q,t) - \Delta S_{\text{exp}}(q,t))}{\sigma_{q,t}} \right)^2 \end{aligned} \quad (22)$$

The global fitting optimizes the rate constants for all reactions, the fraction of excited molecules, the fraction of reacted molecules among excited molecules, the size of the laser spot, and the fraction of the vibrational cooling process. After minimization of chi squared for all time delays, the global-fitting process provides, as a function of time, chemical population changes and the temperature and density changes of the solvent. The overall scheme for the reduction and analysis of TRXL data is presented in Figure 9.

3. X-ray Fingerprinting of Intermediates

TRXL has been used to capture the molecular structures of intermediates and their reaction kinetics for various photochemical processes. In the following, we present several application examples that illustrate the rich variety of observables from TRXL. Four different types of molecular systems have been

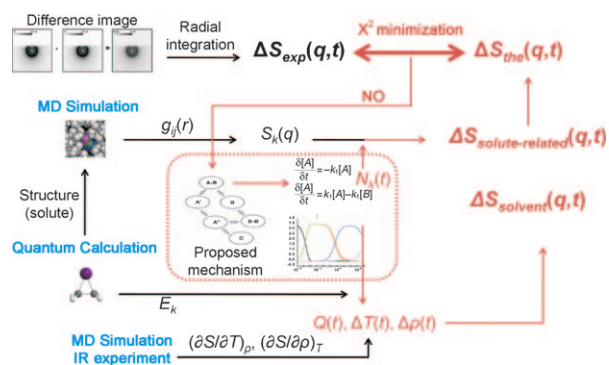


Figure 9. Global-fitting analysis of TRXL data. After radial integration of the diffraction images, the difference curves are obtained after suitable scaling at high scattering angles. Theoretical curves for the solute-related terms are calculated using the $g_{ij}(r)$ functions from MD with putative solute structures from quantum chemical calculations. In the global-fitting analysis, theoretical difference curves, at all time delays, are calculated for a given solute reaction including the hydrodynamic associated with that reaction (energy conservation). Eventually the global fitting minimizes the difference between the theoretical and experimental curves at all times simultaneously, and provides the population of all the chemical species and the temperature, pressure, and density of the solvent environment as a function of time.

studied, simple molecules,^[28,29,31–35] organometallic complexes,^[30] nanoparticles, and proteins, covering a variety of structural problems in photochemistry. We emphasize here the determination of structures of transient intermediates, their cage structures, and the reaction kinetics.

3.1. Spatiotemporal Kinetics of Photoreaction

The photodissociation dynamics of HgI_2 in the gas and solution phases has been widely studied by various time-resolved spectroscopic techniques.^[29] Zewail and co-workers studied two-body dissociation by using laser-induced fluorescence monitoring,^[61] and both two- and three-body dissociation have been measured by time-resolved mass spectrometry.^[62] In the solution phase, the solvation dynamics of HgI_2 in ethanol has been investigated by femtosecond absorption spectroscopy.^[63–65] The vibrational relaxation and rotational dynamics of HgI_2 generated after impulsive dissociation have been discussed. Despite ample information about the dynamics on short time-scales, a comprehensive mechanism spanning from picoseconds to microseconds has been lacking. We applied TRXL to HgI_2 and demonstrated that TRXL provides this information directly. Figure 10a shows the experimental and theoretical intensities $q\Delta S(q)$. Figure 10b shows the corresponding experimental and theoretical difference radial intensity $r\Delta S(r)$. During global-fitting analysis, we used two-body dissociation ($\text{HgI}_2 \rightarrow \text{HgI} + \text{I}$) as the primary dissociation pathway and optimized the rate constants for two-body dissociation, geminate and nongeminate recombination to HgI_2 , nongeminate formation of molecular iodine, and included the laser beam size for the hydrodynamics. The best fits are shown in Figure 10a and b. The fitted theoretical curves successfully reproduce experimental curves in both q and r space. The global-fitting analysis pro-

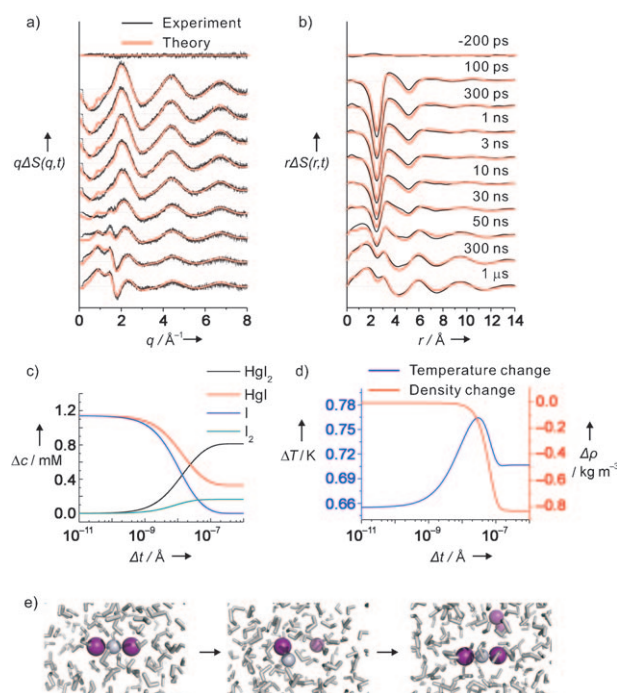


Figure 10. TXRL signals and fitting results for HgI_2 in methanol. a) Experimental (black) and theoretical (red) difference intensities $q\Delta S(q)$ and their error bars in q space. The time delays from top to bottom are -100 ps, 100 ps, 300 ps, 1 ns, 3 ns, 10 ns, 30 ns, 50 ns, 300 ns, and 1 μs . b) Difference RDFs, $r\Delta S(r)$. Shown are the sine-Fourier transforms of the intensities in (a). c) Concentration change of the photoreaction of HgI_2 versus time. HgI , I , I_2 , and HgI_2 are displayed in red, blue, green, and black lines, respectively. d) Change in the solvent density (red) and temperature (blue) as a function of time. Note the duality between the decay in the excited-state population in (c) and the rise in temperature in (d). e) Schematic reaction mechanism by TRXL for the photoreaction of HgI_2 . Pictures for the reaction mechanism are snapshots from MD simulations.

vides, as a function of time, population changes of all chemical species (Figure 10c) and temperature and density changes of the solvent (Figure 10d). Figure 10e summarizes the results. With 267 nm photoexcitation, $(34 \pm 3.8)\%$ of the excited HgI_2 dissociates into $\text{HgI} + \text{I}$. Then $(71 \pm 1.2)\%$ of the transient HgI radical recombines nongeminately with atomic iodine that escaped from other cages to re-form HgI_2 . On the other hand, $(29 \pm 0.5)\%$ of the iodine atoms recombine to form I_2 . The rate constants for the nongeminate recombination of HgI_2 and I_2 were determined to be $(5.0 \pm 0.5) \times 10^{10}$ and $(1.65 \pm 0.25) \times 10^{10} \text{ M}^{-1} \text{ s}^{-1}$, respectively.^[66]

Before the thermal expansion starts, the solute dynamics alone dominates over the cage (solute–solvent term) and solvent terms because of the heavy atoms (Hg and I) in the solute. In Figure 11a and b, the decomposition into solute, cage, and solvent contributions after 100 ps is shown. In the global fitting, the total difference signal is decomposed into these contributions. As expected, the signal from the solute dominates over the entire q range; however, the contributions from the cage and the solvent are not negligible at low q (Figure 11a). In Figure 11b, the negative peak around 2.6 \AA is mainly due to the depletion of the Hg–I bond in HgI_2 and formation of a new Hg–I bond in transient HgI .

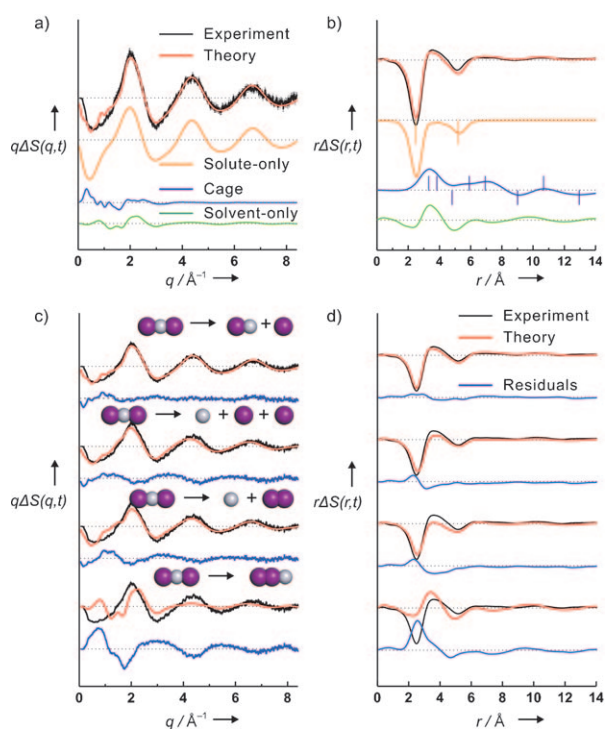


Figure 11. Contributions from the solute-only, solute–solvent (cage), and solvent–solvent correlations to the difference intensities and the difference RDFs for Hgl_2 in methanol at 100 ps. The curve fitting is based on MD and experimental solvent differentials and includes intramolecular and intermolecular contributions from the solutes and the solvent. The experimental (black, with experimental errors) and theoretical (red) $q\Delta S(q)$ (a) and corresponding $r\Delta S(r)$ (b) at 100 ps are shown. Also given are the decomposed components: solute without cage (orange), cage effects (blue), and solvent contribution (green). Decomposed components of cage effects (blue) and the solvent contribution (green) in (b) are multiplied by a factor of 3 to magnify major peaks and valleys. c) Determination of the photodissociation pathway of Hgl_2 in methanol at 100 ps. Theoretical (red) and experimental (black) difference intensities for candidate channels are shown as $q\Delta S(q)$ curves (c) and $r\Delta S(r)$ curves (d). The difference residuals between theoretical and experimental curves are shown in blue. The two-body dissociation pathway ($\text{Hgl}_2 \rightarrow \text{Hgl} + \text{I}$) gives the best fit.

The negative peak near 5.3 \AA corresponds to the I...I distance in the parent molecule. The positive peak at 3.5 \AA is assigned to a reorganization of the solvent around the truncated solute (new cage) and also to solvent heating, which leads to broadening of the methanol–methanol distance. These interpretations can help in determining the primary reaction pathway in the photodissociation of Hgl_2 in solution as follows. Four pathways were considered: $\text{Hgl}_2 \rightarrow \text{Hgl} + \text{I}$, $\text{Hgl}_2 \rightarrow \text{Hg} + \text{I} + \text{I}$, $\text{Hgl}_2 \rightarrow \text{Hg} + \text{I}_2$, and the linear isomer reaction $\text{Hgl}_2 \rightarrow \text{Hgl}-\text{I}$. The data at early times (100 ps, 300 ps, and 1 ns) are fitted globally using the above primary reaction pathways. Figure 11 c and d show comparisons of the fitted results for $q\Delta S(q)$ and $r\Delta S(r)$ for these trial pathways. We can now rule out isomer formation because of the poor agreement between experiment and theory. The fit for the two-body dissociation pathway matches perfectly the experimental data over the entire q range and gives the smallest χ^2 value as compared to the other channels. The fits for the three-body dissociation and I_2 formation channels have a rather good figure of merit, but the fits are worse

than that for the two-body case. In fact, in the fits for these channels, the disagreements are significant for the positive peak at 2 \AA^{-1} and the negative peak at 3 \AA^{-1} . As shown in Figure 11 a, the contribution from the solvent is not negligible. Thus, the apparent disagreements in this region for these two channels clearly indicate that the solvent contribution from these channels is not consistent with the actual energy transfer to the solvent. This tells us that when energetics is considered in the analysis, the solvent contribution can help to discriminate between candidate channels with very small differences at high q . These results clearly demonstrate that TRXL determines concurrently the structures of excited solutes in their cages and the structure and hydrodynamics of the solvent. It is also shown that TRXL can be used as an ultrafast calorimeter, since the determination of transient structure (the primary dissociation channel) is strongly correlated with the energy transfer from solute and solvent molecules.

3.2. Elucidation of the Structure of Transient Species

Halogen elimination reactions from haloalkane are of particular interest since the reaction products are under a stereochemical control related to the final positions of the functional groups with respect to the newly formed C=C double bond.^[67–70] Haloethyl radicals, such as $\text{CH}_2\text{ICH}_2^{\cdot}$ and $\text{CF}_2\text{ICF}_2^{\cdot}$, form as intermediates of the halogen elimination reactions, and their structures have been hypothesized to account for the observed stereoselectivity. In a symmetrically bridged structure, the halogen is shared equally between the two carbon atoms, whereas in a classical mixed structure (a mixture of *anti* and *gauche* conformers) the primary halide resides predominantly on one carbon atom.^[70] A bridged structure of the intermediate prevents rotation about the C–C bond, thereby maintaining the functional group positions in the final product and providing stereochemical control. However, despite numerous theoretical and experimental investigations on these reactions, the structure of the intermediate in solution remained unknown. To unravel the structure of the intermediate and the related kinetics of this reaction, we applied TRXL to the iodine elimination reactions of 1,2-diiodoethane ($\text{C}_2\text{H}_4\text{I}_2$) and 1,2-tetrafluoroiodoethane ($\text{C}_2\text{F}_4\text{I}_2$) dissolved in methanol.^[28,33]

To explain the experimental data theoretically and fit the signals globally, we included all putative structures in the global-fitting processes for both molecules. Our TRXL work has shown that the iodine elimination reactions in $\text{C}_2\text{H}_4\text{I}_2$ and $\text{C}_2\text{F}_4\text{I}_2$ are completely different (Figure 12 c and e for $\text{C}_2\text{H}_4\text{I}_2$ and Figure 12 d and f for $\text{C}_2\text{F}_4\text{I}_2$). The global-fitting results for iodine elimination in $\text{C}_2\text{H}_4\text{I}_2$ show that $\text{C}_2\text{H}_4\text{I}$, I, and the $\text{C}_2\text{H}_4\text{I}-\text{I}$ isomer are the dominant species after 100 ps and the formation of C_2H_4 or I_2 is not observed. $\text{C}_2\text{H}_4\text{I}$ does not decay into $\text{C}_2\text{H}_4 + \text{I}$; rather it reacts with an iodine atom to form an isomer, $\text{C}_2\text{H}_4\text{I}-\text{I}$, with a bimolecular rate constant of $(7.94 \pm 3.48) \times 10^{11} \text{ M}^{-1} \text{ s}^{-1}$,^[66] which is larger by two orders of magnitude than the rate constant for nongeminate recombination of molecular iodine in CCl_4 solvent.

This finding suggests that the isomer is mostly formed via in-cage recombination. The isomer, which is the major species

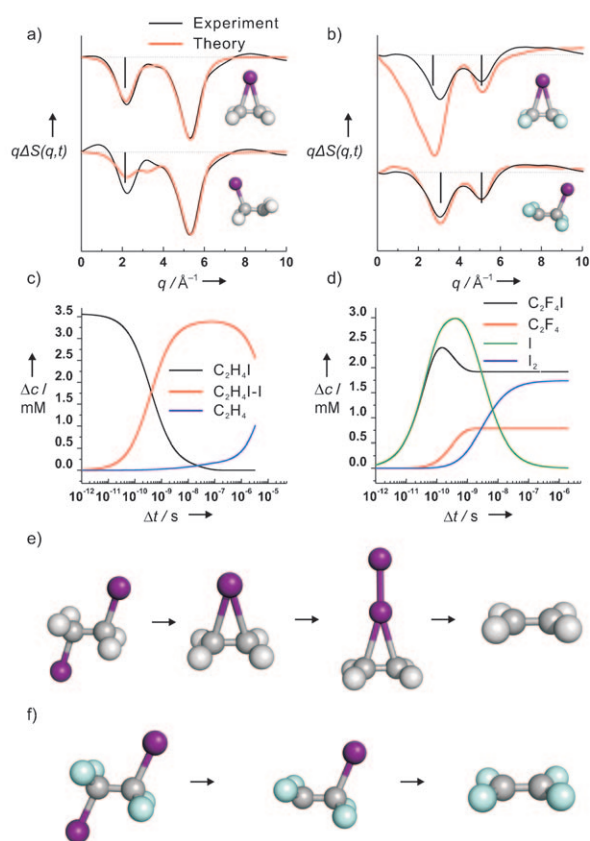


Figure 12. a) Structural determination of the 100 ps C_2H_4I radical in methanol. The C_2H_4I signal is obtained by subtracting other contributions from the raw data. This approach allows comparison of the solution structure with gas-phase structures of the *anti* and bridged conformers. Experimental (black) and theoretical (red) RDFs for the two channels are shown together with their molecular structure (I: purple, C: gray and H: white). The upper and lower curves represent the bridged and classical *anti* structures, respectively. b) Structure determination of the 100 ps C_2F_4I radical in methanol. The solute-only term for the two candidate models (classical and bridged) are shown together with their molecular structure (I: purple, C: gray, and F: cyan). The data show that the C_2H_4I and C_2F_4I radicals have the bridged and classical mixture structure, respectively. c,d) Reaction kinetics and population changes of the relevant chemical species during the photoelimination reaction for $C_2H_4I_2$ (c) and $C_2F_4I_2$ (d) in methanol as a function of time. In (c), black is bridged C_2H_4I , red is the isomer, and blue is the final product C_2H_4 . In (d), green is the I atom, black is the classical form of C_2F_4I , red is C_2F_4 , and blue is the I_2 molecule. e) Reaction model of $C_2H_4I_2$. After photoexcitation, one I atom is detached from the parent molecule, and the C_2H_4I radical is bridged. Then C_2H_4I recombines with another I atom to form a linear isomer C_2H_4I-I . Then the isomer breaks into C_2H_4 and I_2 . f) Reaction model of $C_2F_4I_2$. After photoexcitation, one I atom is detached from the parent molecule, and C_2F_4I takes the classical *anti* form. Some C_2F_4I decays into $C_2F_4 + I$. The I atoms finally recombine nongeminately into I_2 .

in the nanoseconds regime, eventually decays into $C_2H_4 + I_2$ in microseconds with a rate constant of $(1.99 \pm 1.38) \times 10^5 M^{-1} s^{-1}$.^[66] By contrast, C_2F_4I and I are major species at 100 ps as they are essentially formed within a few picoseconds; $(20 \pm 1.3)\%$ of the C_2F_4I radicals decay to $C_2F_4 + I$ with a time constant of (306 ± 48) ps. We can compare these values with those for gas-phase electron diffraction: $(55 \pm 5)\%$ and (26 ± 7) ps.^[11,15] This illustrates how solvent molecules greatly reduce the rate and yield of secondary dissociation. That is not surprising, as the available internal energy of the C_2F_4I radical

in solution is lower than in the gas phase due to the energy transfer to the solvent, which typically occurs in tens of picoseconds. Molecular iodine I_2 is formed concurrently by recombination of two iodine atoms in about 100 ns with a time constant of $(4.4 \pm 1.25) \times 10^{10} M^{-1} s^{-1}$,^[66] which is comparable with the rate constant for nongeminate recombination of molecular iodine in solution.

Of particular interest in these molecule systems is the structure of the transient species. As mentioned, TRXL was the only method that could answer the important question of whether the radical is bridged or classically open. We can calculate the diffraction patterns from putative intermediates and compare those with the solvent-corrected experimental ones. The results from this approach for $C_2H_4I_2$ and $C_2F_4I_2$ are shown in Figure 12a and b, respectively. The transient species alone are found by subtracting the contributions from the solvent, cage, and other nascent solutes and are then compared with calculated candidate molecules. This fingerprint approach is identical to that used in gas-phase time-resolved electron diffraction. The comparison between the 100 ps data and the putative intermediates demonstrates that the C_2H_4I radical has a bridged structure, whereas C_2F_4I is a mixture of a classical *gauche* and an *anti* conformer. In C_2H_4I , the negative peak at 5 Å, the depletion of the I...I distance in the parent molecule, is common for both models. The peaks between 1 and 3 Å are indeed dependent on the position of the I atom relative to the two carbon atoms in the transient intermediate. Only the bridged structure matches the experimental peaks. Note that the *anti* model has two peaks in this fingerprint region from the two different C...I distances. For the C_2F_4I structure, the broad peak between 2 and 4 Å is the fingerprint region. Only the classical mixture structure of C_2F_4I reproduces the broad negative peak in the fingerprint region. The position and line shape of the 3 Å peak are very sensitive to the position of the iodine atom relative to the two carbon atoms and the four fluorine atoms in the transient. Another argument for this structure assignment comes from the χ^2 values from the global fits for the two models. In the elimination reaction of $C_2F_4I_2$, the χ^2 value for the classical mixture is 1.7, which is smaller than the χ^2 value of 3.2 for the bridged structure at all time delays. When both models (bridged and classical mixture) are included in the global fits, the bridged fraction is almost zero. These findings strongly suggest that C_2H_4I is a bridged intermediate whereas C_2F_4I is a classical mixture, and support the fluorination effect on the radical that was predicted by quantum mechanical calculations.

3.3. Revealing Global and Major Reaction Pathways

In principle, diffraction probes the relative positions of all atom–atom pairs in the sample, which implies that no reaction pathway escapes detection to within the limits of the signal-to-noise ratio. In general, diffraction signals from all species are mixed in all diffraction angles whereas in the case of optical spectroscopy, signals from different species can be well resolved in the wavelength regime. Although diffraction offers lower sensitivity to those specific species and specific reaction

channels, the diffraction signals “integrate” all pathways and, in particular, the major channels. Therefore, TRXL provides a global picture of reaction kinetics with reliable branching ratios at the expense of sensitivity. The following examples, the photodissociation dynamics of iodoform (CHI_3) and carbon tetrabromide (CBr_4) in solution, stress this aspect of TRXL.^[30,32]

The photodissociation dynamics of dihaloalkane and trihaloalkane in solution have been extensively investigated by theoretical and experimental methods. The main interest in these systems is the formation of a photoisomer upon UV excitation of low-lying electronic states. For example, iodoform dissociates into CHI_2 and I radicals upon excitation at 350 nm and isoiodoform ($\text{CHI}_2\text{-I}$) is reported to form via in-cage recombination of the photofragments, with a time constant of 7 ps. Previous studies with several time-resolved spectroscopic techniques,^[71,72] such as transient absorption and Raman spectroscopy, suggest that isoiodoform is the major species with a quantum yield of ~ 0.5 in polar solvents (acetonitrile) and ~ 0.4 in nonpolar solvents (cyclohexane) and with lifetimes of microseconds (acetonitrile) and hundreds of nanoseconds (cyclohexane). To probe the formation of isoiodoform and the following dynamics, we applied TRXL to the photodissociation of iodoform in methanol. Figure 13a and b show the experimental $q\Delta S(q)$ and $r\Delta S(r)$ curves and the corresponding theoretical fits. To unravel the formation of isoiodoform, we tested two separate models: simple two-body dissociation ($\text{CHI}_3 \rightarrow \text{CHI}_2 + \text{I}$) and isomer formation ($\text{CHI}_3 \rightarrow \text{CHI}_2\text{-I}$). The χ^2 value for simple dissociation is nine times smaller than the isomer channel at 10 ns, as shown in Figure 13c and d. So isomer formation is not in agreement with the experimental data at all. Moreover, when both models are included in the analysis, the contribution from the isomer channel is negligible. DFT-optimized structures were used for all the putative species. The isomer has three I–I distances (3.616, 3.304, and 6.181 Å), and the C–I angle is 134° . To check the possibility of isomers with other C–I angles, we varied the C–I angle from 134 to 90° in the analysis. However, none of them fitted our experimental data. This result indicates that isomer formation is not a major channel over the investigated time range from 100 ps to 3 μs , which conflicts with the results from time-resolved optical spectroscopy. Figure 13e shows the reaction mechanism found by TRXL. Upon excitation at 266 nm, iodoform dissociates promptly into CHI_2 and I. Molecular iodine (I_2) is formed by nongeminate recombination with a time constant of $(1.55 \pm 0.25) \times 10^{10} \text{ M}^{-1} \text{ s}^{-1}$.^[66] Other photoproducts, such as CHI_3 and $\text{CHI}_2\text{-CHI}_2$, formed by nongeminate recombination are not observed. The example demonstrates that TRXL offers an unbiased method for capturing the major intermediate and its dynamics, which may not be resolved by optical spectroscopy. Although the spectroscopic results indicated the existence of an isoiodoform species with a subnanosecond lifetime, our TRXL data do not show any signal from this intermediate over the investigated time range. The concentration of isoiodoform might be too low to be detected by TRXL with the current signal-to-noise ratio. In addition, the formation of isoiodoform at times below our 100 ps time resolution cannot be ruled out.

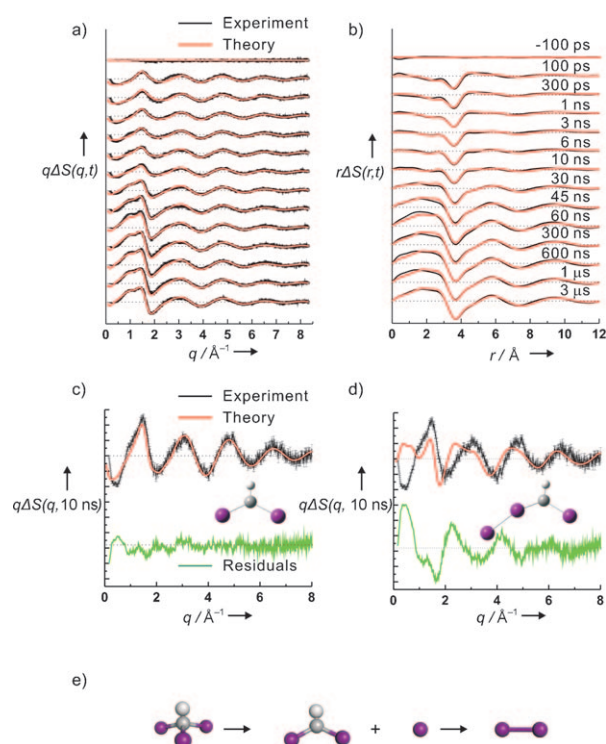


Figure 13. a) Global fits in reciprocal space. Experimental (black) and theoretical (red) data for the photodissociation reaction of CHI_3 in methanol. From top to bottom the time delay of each curve is -100 ps, 100 ps, 300 ps, 1 ns, 3 ns, 6 ns, 10 ns, 30 ns, 45 ns, 60 ns, 300 ns, 600 ns, 1 μs , and 3 μs . b) Global fits in real space. c) Fitting result for the formation of CHI_2 and I at 10 ns. The molecular structure of CHI_2 is also shown (I: purple and C: gray). d) Fitting result for the formation of $\text{CHI}_2\text{-I}$ isomer at 10 ns. The molecular structure of the isomer is also shown (I: purple and C: gray). Black is experiment, red is theory, and green is residuals. The isomer fit is much worse than that with simple two-body dissociation. When both channels are included in the fit, the isomer population converges to zero. e) Reaction mechanism for the photodissociation of iodoform as determined by TRXL.

Carbon tetrahalides are important sources of reactive halogens that have been linked to ozone depletion in the troposphere and stratosphere, and their photochemistry in the gas and solution phases has therefore become an active area of experimental interest.^[73–75] Studies of the photodissociation of CBr_4 by time-resolved optical and X-ray absorption spectroscopy have led to contradictory results. The time-resolved Raman spectroscopic study showed that the $\text{Br}_2\text{CBr-Br}$ isomer is formed upon UV excitation with a lifetime of several nanoseconds.^[76] By contrast, time-resolved absorption spectroscopy measurements indicated that excitation of CBr_4 at 266 nm in various polar and nonpolar solvents results in the formation of a solvent-stabilized ion pair $(\text{CBr}_3^+//\text{Br}^-)_{\text{solvated}}$ with decay constants from subnanoseconds to microseconds dependent on the solvent.^[74] The time-resolved extended X-ray absorption fine structure (EXAFS) study of CBr_4 in cyclohexane did not show any photodissociated reaction intermediate.^[75] These discrepancies indicate that it would be useful to check CBr_4 in solution with the TRXL method because of its global sensitivity, as demonstrated with CHI_3 above.

We have applied TRXL to CBr_4 in methanol (Figure 14). The global-fitting analysis showed the existence of new intermedi-

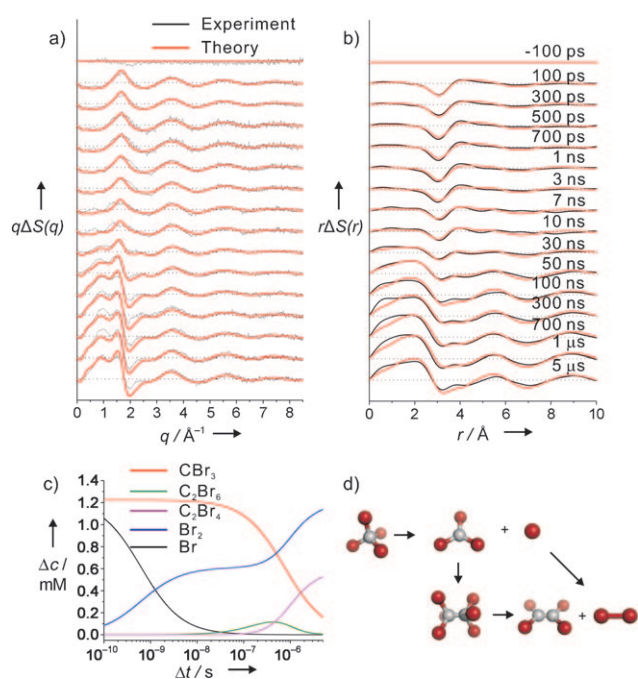


Figure 14. a) Experimental data (black) and global fitting (red) in q space from the photodissociation of CBr_4 in methanol. From top to bottom, the time delay of each curve is -100 ps, 100 ps, 300 ps, 500 ps, 700 ps, 1 ns, 3 ns, 7 ns, 10 ns, 30 ns, 50 ns, 100 ns, 300 ns, 700 ns, 1 μs , and 5 μs . b) Experimental data (black) and the global fitting (red) in r space. c) Population change for each species as a function of time. Red is CBr_3 , olive is C_2Br_6 , magenta is C_2Br_4 , black is the Br atom, and blue is Br_2 . d) Schematic diagram of the photodissociation reaction pathways of CBr_4 in methanol determined by TRXL.

ates that have not been observed in spectroscopic measurements. CBr_3 and Br are the dominant species at early times (~ 100 ps), thus indicating that the C–Br bond is broken in CBr_4 upon UV excitation. The Br radical rapidly decays into Br_2 by nongeminate recombination with a rate constant of $(0.65 \pm 2.3) \times 10^{10} \text{ M}^{-1} \text{ s}^{-1}$.^[66] Most of the CBr_3 radicals decay back to CBr_4 through bimolecular recombination with Br. The main reaction of the CBr_3 radical is escape from the solvation cage and teaming up with another CBr_3 radical to produce C_2Br_6 with a rate constant of $(0.55 \pm 1.3) \times 10^9 \text{ M}^{-1} \text{ s}^{-1}$,^[66] which is an order of magnitude slower than the recombination of two Br atoms into Br_2 . This finding can be rationalized by the relative size of the Br and CBr_3 radicals. The $\text{Br}_2\text{CBr}-\text{Br}$ isomer mentioned previously, formed either by geminated recombination in the cage or by the formation of an ion pair,^[74,76] cannot be observed with the current signal-to-noise ratio, which indicates that these pathways are minor compared to those observed by TRXL. DFT calculation results show that the bimolecular recombination of CBr_3 is exothermic and C_2Br_6 can be produced without an energy barrier. However, the concentration of C_2Br_6 does not correlate with the decays of CBr_3 , which indicates that C_2Br_6 is not stable and dissociates quickly. According to our global fits, C_2Br_6 eventually decays to Br_2 and a new species, C_2Br_4 , as the final photoproducts in microseconds with a rate constant of $(2.9 \pm 3.3) \times 10^6 \text{ s}^{-1}$.^[66] As the CH_3 and CBr_4 examples have shown, X-ray diffraction offers an important ad-

vantage: the scattered X-rays contain contributions from all chemical species within the sample simultaneously.

3.4. Unravelling New Intermediate Species

The TRXL method was applied to the solution-phase photochemistry of the transition-metal photocatalyst $\text{Ru}_3(\text{CO})_{12}$ and the binuclear complex $[\text{Pt}_2(\text{P}_2\text{O}_5\text{H}_2)_4]^{4-}$ (PtPOP). These molecules were selected as ideal targets due to their high scattering power and interesting photophysical and photochemical properties.

The triangular metal carbonyl cluster $\text{Ru}_3(\text{CO})_{12}$ is widely used as a catalyst in controlled photoactivated synthesis in which specific bonds in the complex can be broken selectively at specific (excitation) wavelengths.^[77,78] The rearrangement and decomposition of $\text{Ru}_3(\text{CO})_{12}$ are not only of fundamental interest but also of great practical importance. For this reason the photolysis of $\text{Ru}_3(\text{CO})_{12}$ in solution has been extensively investigated with various spectroscopic tools.^[78–86] Ultrafast infrared spectroscopic measurements show that photoexcited $\text{Ru}_3(\text{CO})_{12}$ in a noncoordinating solvent such as cyclohexane produces two types of transient intermediates containing bridging carbonyl ligands: $\text{Ru}_3(\text{CO})_{11}(\mu\text{-CO})$ (intermediate 1) from the metal–metal cleavage channel and $\text{Ru}_3(\text{CO})_{10}(\mu\text{-CO})$ for the CO loss reaction pathway (intermediate 2).^[86] In this study, the dynamics of these intermediates can only be unambiguously identified by monitoring the distinct infrared absorption from the bridging carbonyl groups. However, this leaves the possibility of missing other intermediates, especially those with only terminal carbonyls where the absorption bands overlap with those of the parent molecule (Figure 15a). To address this issue, we applied TRXL to the dissociation of $\text{Ru}_3(\text{CO})_{12}$ in cyclohexane photoexcited at 390 nm in the low-energy band (Figure 15b).^[30]

Initial fits with intermediates 1 and 2 failed, which implies the existence of other intermediates. According to previous spectroscopic studies, the decay times of intermediates 1 and 2 are 150 ps and 5 ns, respectively, and therefore the signal at longer time delays should be dominated by the new intermediate. Thus, we fitted the experimental data at 30 ns with the Debye scattering curves from putative structural transitions (Figure 15c). The reaction pathway $\text{Ru}_3(\text{CO})_{12} \rightarrow \text{Ru}_3(\text{CO})_{10} + 2\text{CO}$ matches the experimental data well over the entire q range. The data analysis shows that the primary photoproduct is the $\text{Ru}_3(\text{CO})_{10}$ isomer. Only this isomer, with terminal carbonyl groups only (intermediate 3), reproduces the experimental signal whereas the other isomers, with bridging carbonyl ligands, do not match the signal. This finding suggests that the ultrafast infrared spectroscopic studies missed intermediate 3 due to the absence of bridging carbonyl ligands.

To explain the time-resolved experimental data and to extract the overall spatiotemporal kinetics, we performed global-fitting analysis by including the parent and intermediates 1–3. Figure 15d shows the concentration changes of the relevant chemical species, as a function of time, determined by global-fitting analysis. After photoexcitation of $\text{Ru}_3(\text{CO})_{12}$, intermediate 1 [$\text{Ru}_3(\text{CO})_{11}(\mu\text{-CO})$] is formed from the metal–metal cleav-

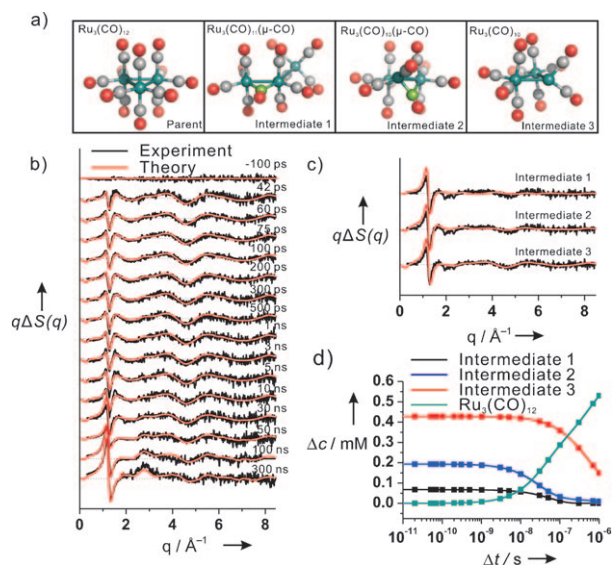


Figure 15. a) Molecular structure and intermediates in the photoreaction of $\text{Ru}_3(\text{CO})_{12}$. Intermediate 1 is the result of Ru–Ru bond breaking, intermediate 2 is the result of CO dissociation, and intermediate 3 is from dissociation of two CO groups. b) Comparison of experimental data (black) and theoretical data (red) in q space. The time delays from top to bottom are –100 ps, 42 ps, 60 ps, 75 ps, 100 ps, 200 ps, 300 ps, 500 ps, 1 ns, 3 ns, 5 ns, 10 ns, 30 ns, 50 ns, 100 ns, and 300 ns. The values in the low- q region of the first 13 curves and the last three curves have been divided by 3 and 6, respectively, for clarity. c) Determination of the photoproducts at 30 ns and characterization of intermediate 3. Experimental (black) and theoretical (red) difference scattering intensities $q\Delta S(q)$ for various candidate reactions (top: intermediate 1, middle: intermediate 2, and bottom: intermediate 3) are shown. Intermediate 3 gives the best agreement between experiment and theory. d) Concentration change of the photoreaction of $\text{Ru}_3(\text{CO})_{12}$ (black: intermediate 1, blue: intermediate 2, red: intermediate 3, and cyan: $\text{Ru}_3(\text{CO})_{12}$). Within the time resolution of 100 ps, three intermediates are observed and they return to the parent molecule.

age channel and decays exponentially to the initial $\text{Ru}_3(\text{CO})_{12}$ with a unimolecular rate constant of $(1.68 \pm 1.69) \times 10^7 \text{ s}^{-1}$.^[66] As this intermediate is a minor species (Figure 15d), the error is rather large unfortunately. Actually a reasonable fit can be simulated without intermediate 1. On the contrary, intermediate 2 [$\text{Ru}_3(\text{CO})_{11}(\mu\text{-CO})$], which is formed from the CO-loss channel, is necessary to generate a reasonable fit. This intermediate recombines nongeminately with CO to give the parent molecule with a bimolecular rate constant of $(3.27 \pm 0.19) \times 10^{10} \text{ M}^{-1} \text{ s}^{-1}$.^[66] The major species, intermediate 3 [$\text{Ru}_3(\text{CO})_{10}$], decays into intermediate 2 by nongeminate recombination with CO with a rate constant of $(1.88 \pm 0.08) \times 10^9 \text{ M}^{-1} \text{ s}^{-1}$.^[66] As the decay of intermediate 3 is much slower than that of intermediate 2, any

intermediate with the formula $\text{Ru}_3(\text{CO})_{11}$ is a candidate for the actual intermediate formed from nongeminate recombination of intermediate 3 and CO. Therefore, the structure of the intermediate that connects intermediate 3 and the parent molecule cannot be determined. Since the Ru–Ru distances contribute more than 90% to the coherent diffraction signal, an attempt was made to optimize all the Ru–Ru distances in the parent molecule and in the transient intermediates, by using a single scale factor for the calculated Ru–Ru distances. The optimized experimental bond lengths are shorter than those from DFT, consistent with the general trend of DFT calculations to overestimate the metal–metal distance. The $\text{Ru}_3(\text{CO})_{12}$ case demonstrates that TRXL and ultrafast optical spectroscopy are complementary with each other. Intermediate 3 is invisible in infrared spectroscopy, but has to be included in the TRXL data. On the other hand, TRXL alone cannot determine the existence of a minor species such as intermediate 1, since its contribution to the overall diffraction is so weak compared to that of intermediate 3. Therefore, the results from the two complementary techniques indicate the existence of at least three intermediates with very different molecular structures and time constants.

TRXL has also been used to study the excited-state structure of the organometallic compound PtPOP. PtPOP has D_{4h} symmetry with a square-planar configuration around two platinum atoms (Figure 16a). As in other binuclear d^8 complexes, the lowest electronic excitation is $\sigma^* \rightarrow \sigma$ which results in a large contraction along the metal–metal coordinate. The lowest excited state of PtPOP has ${}^3A_{2u}$ symmetry. The lifetime of the lowest excited state is determined to be 9.8 μs in deoxygenated water.^[87] The quantum yield of 100% for triplet formation in the upper states is also derived from photophysical data.^[88] Several methods have been applied to characterize the structural parameters of the lowest excited state. Time-resolved X-ray absorption fine structure (XAFS) measurements derive $(0.52 \pm 0.13) \text{ \AA}$ inward movements of the P–P planes upon excitation into the ${}^3A_{2u}$ state in water.^[89] An excited-state crystal

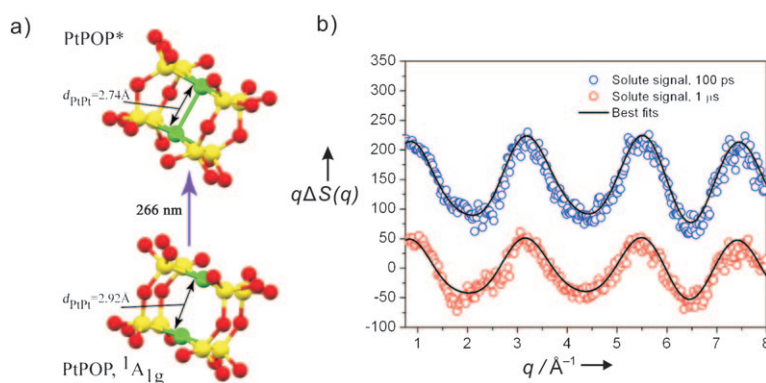


Figure 16. a) Model structures of the PtPOP anion, $[\text{Pt}_2(\text{P}_2\text{O}_5\text{H}_2)_4]^{4-}$, in the ground (${}^1A_{1g}$) and lowest excited (${}^3A_{2u}$) states without hydrogen atoms. The bond distances in both states are displayed. An 8% contraction of Pt–Pt distance occurs upon optical excitation (Pt: green, P: yellow, and O: red). b) Solute-only contributions at 100 ps (blue circles) and 1 μs (red circles) and the fit (black line) from global maximum-likelihood analysis. In the experimental and theoretical data, the bulk-solvent contribution is subtracted to emphasize the contribution to the difference diffraction signal from changes in the molecular structure of the solute. The decrease in the oscillation amplitude corresponds to a lower population of the excited-state PtPOP at 1 μs .

structure at low temperatures has also been determined by time-resolved X-ray diffraction. The Pt–Pt distance of the $^3A_{2u}$ state was measured in a single crystal of $(Et_4N)_3HPtPOP$ at cryogenic temperatures with microsecond time resolution, and a contraction of 0.28 Å was obtained.^[90] Figure 16b shows the solute-only terms of the transient species ($^3A_{2u}$ state) at 100 ps and 1 μ s. Information about key structural parameters is obtained by fitting a simulated difference signal $[\Delta S(q,t)]$ for a range of hypothetical structures to the experimental data and evaluating the quality of the fit. In the present case, the key parameters are the Pt–Pt distance and the distance between the P planes. The analysis shows that the Pt–Pt distance in the $^3A_{2u}$ state is (2.74 ± 0.06) Å, a contraction of 0.24 Å or 8% from the ground-state distance (2.98 Å) from static X-ray diffraction. The contraction due to the optical excitation is in good agreement with earlier values from time-resolved resonance Raman spectroscopy and diffraction data in the crystalline phase and from time-resolved EXAFS measurement in solution.^[91] The distance between the P planes in the $^3A_{2u}$ state is determined to be (2.74 ± 0.06) Å, which is identical to the ground state within experimental accuracy. This finding implies a slight lengthening of the Pt–P bond following excitation.

3.5. Thermal and Structural Dynamics of Photoexcited Nanoparticles

Metal and semiconductor nanoparticles have been extensively investigated due to their nonlinear properties.^[92,93] A large number of ultrafast optical studies have focused on the transient optical properties as a function of material, particle size, and embedding environment.^[92] For example, time-resolved optical pump–probe measurements have shown that the energy absorbed by electrons in metals after ultrafast excitation is transferred to the lattice via phonon emission within a few picoseconds, which leads to a homogeneous temperature distribution in each nanoparticle,^[94,95] and the nanoparticles cool down in less than a nanosecond.^[95] However, it is difficult to address the structural properties by optical spectroscopic methods, especially where nonreversible processes are concerned. Since X-ray scattering is sensitive to all structural relaxations in the sample, TRXL makes it possible to track the structural relaxations in the nanoparticles (heating, melting, and explosion) and in the surround medium (explosive boiling).

Recently, the TRXL method has been applied to gold nanoparticles suspended in water to obtain a time-resolved picture of the structural and thermal dynamics of the nanoparticles and adjacent medium following excitation with femtosecond laser pulses.^[96–100] The signals from the water solvent (wide-angle X-ray scattering, WAXS), the particle lattice (powder scattering), and the shape scattering from nanoparticles (small-angle X-ray scattering, SAXS) were used to determine the structure of the particles as well as that of the local environment (water). By detecting powder scattering from gold nanoparticles as a function of time delay and laser fluence, the transient heating and subsequent matrix cooling dynamics were measured. It was also found that the thermal relaxation can be modeled quantitatively for a range of particle sizes between

10 and 100 nm.^[96] At low excitation fluences, the measurements show regular cooling dynamics with a heat flow from the nanoparticles to the water medium. The thermal conductivity in bulk water and in the particle/water interface affects the cooling process, which lasts for about a nanosecond for larger particles.^[95] By increasing the fluence, the water around the nanoparticles reaches a critical temperature, which leads to explosive evaporation (vapor-bubble formation).^[98–99] These bubbles inhibit the cooling process on the subnanosecond timescale. The nanoscale structure for this process has been resolved directly by TRXL.^[99] The nanoparticles themselves undergo a melting transition and fragment. The fragments form new particles with sizes around 9 Å on the microsecond timescale.^[100] It has been discovered that nonreversible mass removal from gold particles in water can be initiated below the melting point of the particles. By combining different scattering methods in the pump–probe setup (small-angle scattering and powder diffraction), it was shown that the (anisotropic) change in shape of nanoparticles occurs on the picosecond timescale.

3.6. Protein Structural Dynamics

One can envision studying more complex molecules such as proteins by using TRXL. In the case of proteins in physiological media, the relatively low concentration (a few mM or less) makes TRXL measurements extremely difficult and the large molecular size (more than a thousand times larger than small molecules) complicates the structural analysis. However, recent TRXL data from model proteins in solution have demonstrated that the medium- to large-scale dynamics of proteins is rich in information on timescales from nanoseconds to milliseconds.^[101] Due to the inverse relationship between the interatomic distance and the scattering angle, the scattering from macromolecules appears at smaller scattering angles in the SAXS/WAXS range. For this reason, the TRXL method applied to protein samples is termed TR-SAXS/WAXS. The TR-SAXS/WAXS methodology has been applied to human hemoglobin (Hb), a tetrameric protein made of two identical α,β dimers that is known to have at least two different quaternary structures (a ligated stable “relaxed” (R) state and an unligated stable “tense” (T) structure) in solution. The tertiary and quaternary conformational changes of Hb triggered by laser-induced ligand dissociation have been identified with this method. A preliminary analysis by the allosteric kinetic model gives a timescale for the R–T transition of $\sim 1\text{--}3$ μ s, which is shorter than the timescale derived with time-resolved optical spectroscopy. In Figure 17a, gas-phase scattering from the crystal structures of HbCO and Hb (deoxyHb) are shown together with one myoglobin (Mb) unit and a water molecule. In Figure 17b, the relative change from the transition HbCO \rightarrow Hb is shown for a 1 mM concentration. Note the good signal-to-background ratio between 0.1 and 1 \AA^{-1} due to weak scattering on the low- q water “plateau”. Finally, the structures of the proteins and water are shown in Figure 17c. The optically induced tertiary relaxation of Mb and the refolding of cytochrome *c* have also been studied with TR-SAXS/WAXS.^[101] The ad-

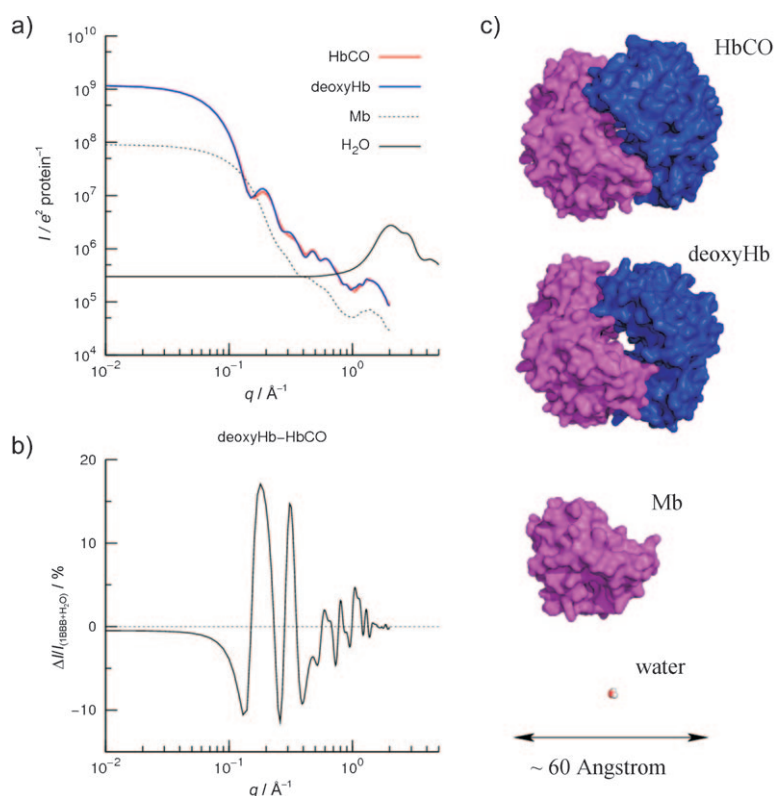


Figure 17. a) Calculated Debye scattering for hemoglobin (HbCO and Hb), myoglobin (Mb), and water. b) Relative change of the protein signal to the water background for the R-to-T transition (HbCO→Hb) for an excited-state concentration of 1 mM. c) Snapshots of molecular structures used in the calculations of the scattering patterns.

vantage of TR-SAXS/WAXS over time-resolved X-ray protein crystallography is that it can probe irreversible reactions, as illustrated by the folding of cytochrome *c*, as well as reversible reactions, such as ligand reactions in heme proteins. Although the diffraction patterns from proteins in solution contain structural information, the information content is probably insuffi-

cient to reconstruct protein structures on atomic scales. In this respect, the use of structures from X-ray crystallography and NMR spectroscopy as a starting point for refinements against TR-SAXS/WAXS data is promising and the development of an accurate theoretical analysis is in progress. The rate constants and lifetimes of all photo-reactions investigated by TRXL are assembled in Table 1.

4. Comparisons with Other Time-Resolved Techniques

4.1. Comparison with Time-Resolved Optical Spectroscopy

To track time-dependent processes, various time-resolved spectroscopic tools have been developed and reaction dynamics with femtosecond time resolution can now be routinely investigated by such methods. Time-resolved optical spectroscopy has been applied to studying ultrafast events in various areas of chemistry, physics, and biology. A laser pulse triggers a photochemical reaction or a perturbation in the system and another laser pulse (with wavelength ranging from the ultraviolet to infrared or far infrared) probes the optical responses of the system as a function of time delay between pump and probe pulses as well as the wavelength of the probe pulse. This method permits the detection of specific short-lived species or energy states with very high sensitivity. Unfortunately, the optical probe is not able to interfere with all atoms and thus experimental observables in optical spectroscopy, such as transition energy and transition intensity, cannot provide direct structural information, such as atomic coordinates or at least bond lengths and bond angles. In contrast, since the X-ray scattering probes all atom-atom pairs in the molecular system, TRXL has unique capabilities to directly access the structural dynamics in the sample. In spite of the diffraction signal in TRXL

Table 1. Rate constants for molecular systems studied by TRXL.

Solute/Solvent	Reaction	Values
C ₂ H ₄ I ₂ /CH ₃ OH	C ₂ H ₄ I + I → C ₂ H ₄ I ^[a]	7.94(±3.48) × 10 ¹¹
	C ₂ H ₄ I-I → C ₂ H ₄ + I ₂ ^[b]	1.99(±1.38) × 10 ⁵
HgI ₂ /CH ₃ OH	HgI + I → HgI ₂ ^[a]	5.0(±0.5) × 10 ¹¹
	I + I → I ₂ ^[a]	1.65(±0.3) × 10 ¹⁰
CHI ₃ /CH ₃ OH	I + I → I ₂ ^[a]	1.55(±0.3) × 10 ¹⁰
	C ₂ F ₄ I ₂ /CH ₃ OH	C ₂ F ₄ I → C ₂ F ₄ + I ^[b]
CBr ₄ /CH ₃ OH	I + I → I ₂ ^[a]	4.4(±1.25) × 10 ¹⁰
	CBr ₃ + CBr ₃ → C ₂ Br ₆ ^[a]	0.55(±1.3) × 10 ⁹
	C ₂ Br ₆ → C ₂ Br ₄ + Br ₂ ^[b]	2.9(±3.3) × 10 ⁶
Ru ₃ (CO) ₁₂ /C ₆ H ₁₂	Br + Br → Br ₂ ^[a]	0.65(±2.3) × 10 ¹⁰
	intermediate 1 → parent ^[b]	1.68(±1.69) × 10 ⁷
	intermediate 2 + CO → parent ^[a]	3.27(±0.19) × 10 ¹⁰
	intermediate 3 + CO → intermediate 2 ^[a]	1.88(±0.08) × 10 ⁹

[a] The values give the reaction constant in m⁻¹ s⁻¹. [b] The values give the reaction constant in s⁻¹.

being less sensitive to a specific transient than optical spectroscopy, its signal allows the direct observation of major transient species and provides a global picture of the reactions with accurate branching ratios between multiple reaction pathways, as shown in the examples in the previous sections. Since X-rays scatter from all atoms in the solution, solutes as well as solvent molecules, the analysis of TRXL data can provide the temporal behavior of the solvent as well as the structural progression of the solute molecules in all their reaction pathways, thus providing information on the rearrangement of the solvent around the transient solutes.

Vibrational transitions in a molecule can often be correlated to specific vibrational motions of a molecule with characteristic vibrational frequencies and can be used to probe specific sites within molecular systems. For this reason time-resolved vibrational (IR and Raman) spectroscopies^[102,103] have been used for probing transient structures in chemical reactions. However, the vibrational signals bias species with high absorption cross section and these techniques may fail to detect optically silent species. In addition, it is often difficult to obtain insight into the global structure from vibrational spectroscopy, and new approaches, such as multidimensional IR and Raman spectroscopies, have emerged which are very promising in this respect.^[104,105] Two-dimensional spectroscopy measures the vibration–vibration coupling between specific vibrational modes, which are correlated with the relative orientation of the molecule. The vibration–vibration coupling is very sensitive to molecular structure by analogy to the spin–spin coupling in two-dimensional NMR spectroscopy. Great progress has been made recently in resolving the molecular dynamics in biological systems by multidimensional spectroscopy.

As shown in the examples in Section 3, time-resolved optical spectroscopy and TRXL complement each other well. The former has a higher sensitivity and is thus useful for detecting extremely dilute reaction intermediates, whereas TRXL provides direct structural information and accurate branching ratios.

4.2. Comparison with Time-Resolved X-ray Absorption Spectroscopy

X-ray absorption spectroscopy, such as X-ray absorption near-edge structure (XANES) and EXAFS, provide local structural information and therefore the local response to laser excitation can be obtained by these methods. The EXAFS region delivers quantitative structural information with sub-Å accuracy via the so-called EXAFS equation,^[48] whereas XANES provides a quantitative fingerprint of the local chemical bonding geometry, such as orbital hybridization, in the vicinity of the atom(s) of interest. This can be useful for understanding molecular dynamics in solution, where much important chemistry occurs, and where the solvent environment substantially influences reaction dynamics. Like TRXL, X-ray absorption spectroscopy has also been used in time-resolved studies with the laser pump and X-ray probe scheme, and has been applied to studying charge-transfer^[48–50,106,107] and spin-crossover processes^[37,108] in coordination chemistry compounds, solvation dynamics of

atomic radicals,^[109] and structural dynamics of photodissociated intermediates in the solution phase.^[107,110] The structural information obtained by X-ray absorption is limited to the local environment of a particular atom. This feature is in contrast to the diffraction method, which provides structural information for all species. The locality of the X-ray absorption signal has the advantage of a much higher sensitivity. In summary, TRXL and time-resolved X-ray absorption spectroscopy are highly complementary and thus, in the future, a combination of the two techniques may prove to be useful in providing more accurate results. Such efforts are in progress within the upgrade program at the ESRF for 2012.

5. Summary and Outlook

In this review we have outlined the experimental and theoretical backgrounds of TRXL and given recent examples from photochemical research of the liquid phase. Although TRXL has limitations, it provides direct structural and kinetic information on the reaction dynamics of chemical reactions in liquids. TRXL addresses detailed information about the structural changes and spatiotemporal kinetics of reaction intermediates in all reaction pathways, temporal rearrangements of solvents around solutes, and the related solvent hydrodynamics. For example, TRXL can aid in the understanding of major reaction pathways, as shown for CH_3 and CBr_4 , the TRXL results for which are different from those with time-resolved optical spectroscopy. TRXL can also identify new intermediates, as illustrated for the photolysis of $\text{Ru}_3(\text{CO})_{12}$, where TRXL complements the results from time-resolved spectroscopy. Moreover, TRXL is capable of providing direct structural information that is difficult to obtain from time-resolved optical spectroscopy, such as the molecular structure of intermediates involved in iodine elimination reactions from $\text{C}_2\text{H}_4\text{I}_2$ and $\text{C}_2\text{F}_4\text{I}_2$. In addition, TRXL has been applied to the investigation of the structural dynamics of more complicated systems, such as nanoparticles and proteins in solution.

Increasing q_{max} from the current $\sim 8 \text{ \AA}^{-1}$ to 12 \AA^{-1} by using harder X-rays will not only provide more data, but will also increase the accuracy of the scaling of RDF curves by giving access to the atomic limit where molecules scatter as the sum of independent atoms without structure. Multilayer X-ray optics to provide X-rays with shorter wavelength (0.50 \AA) is being installed at ESRF on beamline ID09B. Application of the TRXL method to molecules without heavy atoms is a challenge to be overcome. Such systems require that the signal-to-noise ratio of scattering data should be improved. For example, to extract a ten times weaker signal (in general, the scattering signal is proportional to Z^2), the data acquisition time should be increased 100 times. This is unrealistic in current experimental setups, but could be feasible with future X-ray sources with a much higher flux (see below). Chemical substitution with heavy atoms may also provide a solution. The time resolution of TRXL is currently limited by the temporal length of X-ray pulses produced by synchrotron radiation facilities (100 ps). This time resolution might be improved with next-generation sources, such as X-ray free-electron lasers and energy-recovery linacs, which promise to deliver subpicosecond X-ray pulses

with increased photon flux and nearly full coherence. As the proposed ultrafast X-ray facilities (e.g., X-ray free-electron lasers) come online, the time resolution might reach 100 fs and below. It will be possible to image atomic motions along the potential energy surface in real time and to monitor bond breaking/formation and isomerization processes in the solution phase. However, as the X-ray pulses become as short as a few hundreds of femtoseconds or less, assumptions of thermally equilibrated solute structure and hydrodynamic equations for solvent responses will be no longer valid, which could complicate the theoretical analysis of TRXL data and structure determination. As these challenges are overcome, TRXL will have great impact on the study of reaction dynamics.

Acknowledgements

We thank co-workers listed in many of the references of this review. This work was supported by the Creative Research Initiative (Center for Time-Resolved Diffraction) of MEST/KOSEF.

Keywords: liquids · photochemistry · structural dynamics · time-resolved spectroscopy · X-ray diffraction

- [1] A. H. Zewail, *Angew. Chem.* **2001**, *113*, 4501–4506; *Angew. Chem. Int. Ed.* **2001**, *40*, 4371–4375, and references therein.
- [2] N. Biswas, S. Umopathy, *J. Chem. Phys.* **1997**, *107*, 7849–7858.
- [3] P. Kukura, D. W. McCamant, S. Yoon, D. B. Wandschneider, R. A. Mathies, *Science* **2005**, *310*, 1006–1009.
- [4] Y. Mizutani, T. Kitagawa, *Science* **1997**, *278*, 443–446.
- [5] W. J. Schreier, T. E. Schrader, F. O. Koller, P. Gilch, C. E. Crespo-Hernandez, V. N. Swaminathan, T. Carell, W. Zinth, B. Kohler, *Science* **2007**, *315*, 625–629.
- [6] S. Takeuchi, S. Ruhman, T. Tsuneda, M. Chiba, T. Taketsugu, T. Tahara, *Science* **2008**, *322*, 1073–1077.
- [7] S. O. Williams, D. G. Imre, *J. Phys. Chem.* **1988**, *92*, 3363–3374.
- [8] H. Lee, Y. C. Cheng, G. R. Fleming, *Science* **2007**, *316*, 1462–1465.
- [9] J. R. Zheng, K. W. Kwak, J. Xie, M. D. Fayer, *Science* **2006**, *313*, 1951–1955.
- [10] S. Chen, M. T. Seidel, A. H. Zewail, *Proc. Natl. Acad. Sci. USA* **2005**, *102*, 8854–8859.
- [11] H. Ihee, V. A. Lobastov, U. M. Gomez, B. M. Goodson, R. Srinivasan, C. Y. Ruan, A. H. Zewail, *Science* **2001**, *291*, 458–462.
- [12] R. C. Dudek, P. M. Weber, *J. Phys. Chem. A* **2001**, *105*, 4167–4171.
- [13] A. Gahlmann, S. T. Park, A. H. Zewail, *Phys. Chem. Chem. Phys.* **2008**, *10*, 2894–2909.
- [14] B. J. Siwick, J. R. Dwyer, R. E. Jordan, R. J. D. Miller, *Science* **2003**, *302*, 1382–1385.
- [15] H. Ihee, B. M. Goodson, R. Srinivasan, V. A. Lobastov, A. H. Zewail, *J. Phys. Chem. A* **2002**, *106*, 4087–4103.
- [16] J. S. Baskin, A. H. Zewail, *ChemPhysChem* **2005**, *6*, 2261–2276.
- [17] C. Y. Ruan, V. A. Lobastov, F. Vigliotti, S. Y. Chen, A. H. Zewail, *Science* **2004**, *304*, 80–84.
- [18] C. Y. Ruan, D. S. Yang, A. H. Zewail, *J. Am. Chem. Soc.* **2004**, *126*, 12797–12799.
- [19] D. S. Yang, C. S. Lao, A. H. Zewail, *Science* **2008**, *321*, 1660–1664.
- [20] D. Shorokhov, A. H. Zewail, *Phys. Chem. Chem. Phys.* **2008**, *10*, 2879–2893.
- [21] D. S. Yang, N. Gedik, A. H. Zewail, *J. Phys. Chem. C* **2007**, *111*, 4889–4919.
- [22] C. Y. Ruan, Y. Murooka, R. K. Raman, R. A. Muddick, *Nano Lett.* **2007**, *7*, 1290–1296.
- [23] J. Cao, Z. Hao, H. Park, C. Tao, D. Kau, L. Blaszczyk, *Appl. Phys. Lett.* **2003**, *83*, 1044–1046.
- [24] M. Harb, R. Ernstorfer, C. T. Hebeisen, G. Sciaini, W. Peng, T. Dartigalongue, M. A. Eriksson, M. G. Lagally, S. G. Kruglik, R. J. D. Miller, *Phys. Rev. Lett.* **2008**, *100*, 155504.
- [25] H. Ihee, *Acc. Chem. Res.* **2009**, *42*, 356–366.
- [26] M. Cammarata, M. Lorenc, T. K. Kim, J. H. Lee, Q. Y. Kong, E. Pontecorvo, M. Lo Russo, G. Schiro, A. Cupane, M. Wulff, H. Ihee, *J. Chem. Phys.* **2006**, *124*, 124504.
- [27] J. Davidsson, J. Poulsen, M. Cammarata, P. Georgiou, R. Wouts, G. Katona, F. Jacobson, A. Plech, M. Wulff, G. Nyman, R. Neutze, *Phys. Rev. Lett.* **2005**, *94*, 245503.
- [28] H. Ihee, M. Lorenc, T. K. Kim, Q. Y. Kong, M. Cammarata, J. H. Lee, S. Bratos, M. Wulff, *Science* **2005**, *309*, 1223–1227.
- [29] T. K. Kim, M. Lorenc, J. H. Lee, M. Russo, J. Kim, M. Cammarata, Q. Y. Kong, S. Noel, A. Plech, M. Wulff, H. Ihee, *Proc. Natl. Acad. Sci. USA* **2006**, *103*, 9410–9415.
- [30] Q. Y. Kong, J. H. Lee, A. Plech, M. Wulff, H. Ihee, M. H. J. Koch, *Angew. Chem.* **2008**, *120*, 5632–5635; *Angew. Chem. Int. Ed.* **2008**, *47*, 5550–5553.
- [31] Q. Y. Kong, M. Wulff, J. H. Lee, S. Bratos, H. Ihee, *J. Am. Chem. Soc.* **2007**, *129*, 13584–13591.
- [32] J. H. Lee, J. Kim, M. Cammarata, Q. Kong, K. H. Kim, J. Choi, T. K. Kim, M. Wulff, H. Ihee, *Angew. Chem.* **2008**, *120*, 1063–1066; *Angew. Chem. Int. Ed.* **2008**, *47*, 1047–1050.
- [33] J. H. Lee, T. K. Kim, J. Kim, Q. Kong, M. Cammarata, M. Lorenc, M. Wulff, H. Ihee, *J. Am. Chem. Soc.* **2008**, *130*, 5834–5835.
- [34] A. Plech, M. Wulff, S. Bratos, F. Mirloup, R. Vuilleumier, F. Schotte, P. A. Anfinrud, *Phys. Rev. Lett.* **2004**, *92*, 125505.
- [35] M. Wulff, S. Bratos, A. Plech, R. Vuilleumier, F. Mirloup, M. Lorenc, Q. Kong, H. Ihee, *J. Chem. Phys.* **2006**, *124*, 034501.
- [36] I. V. Tomov, P. M. Rentzepis, *ChemPhysChem* **2004**, *5*, 27–35.
- [37] M. Khalil, M. A. Marcus, A. L. Smeigh, J. K. McCusker, H. H. W. Chong, R. W. Schoenlein, *J. Phys. Chem. A* **2006**, *110*, 38–44.
- [38] M. Bargheer, N. Zhavoronkov, M. Woerner, T. Elsaesser, *ChemPhysChem* **2006**, *7*, 783–792.
- [39] A. Cavalleri, M. Rini, H. H. W. Chong, S. Fourmaux, T. E. Glover, P. A. Heimann, J. C. Kieffer, R. W. Schoenlein, *Phys. Rev. Lett.* **2005**, *95*, 067405.
- [40] A. Cavalleri, S. Wall, C. Simpson, E. Stutz, D. W. Ward, K. A. Nelson, M. Rini, R. W. Schoenlein, *Nature* **2006**, *442*, 664–666.
- [41] A. Debnarova, S. Techert, S. Schmatz, *J. Chem. Phys.* **2006**, *125*, 224101.
- [42] S. Techert, F. Schotte, M. Wulff, *Phys. Rev. Lett.* **2001**, *86*, 2030–2033.
- [43] M. Gembicky, P. Coppens, *J. Synchrotron Radiat.* **2007**, *14*, 133–137.
- [44] I. I. Vorontsov, A. Y. Kovalevsky, Y. S. Chen, T. Graber, M. Gembicky, I. V. Novozhilova, M. A. Omary, P. Coppens, *Phys. Rev. Lett.* **2005**, *94*, 193003.
- [45] H. Ihee, S. Rajagopal, V. Srajer, R. Pahl, S. Anderson, M. Schmidt, F. Schotte, P. A. Anfinrud, M. Wulff, K. Moffat, *Proc. Natl. Acad. Sci. USA* **2005**, *102*, 7145–7150.
- [46] V. Schmidt, R. Pahl, V. Srajer, S. Anderson, Z. Ren, H. Ihee, S. Rajagopal, K. Moffat, *Proc. Natl. Acad. Sci. USA* **2004**, *101*, 4799–4804.
- [47] F. Schotte, M. H. Lim, T. A. Jackson, A. V. Smirnov, J. Soman, J. S. Olson, G. N. Phillips, M. Wulff, P. A. Anfinrud, *Science* **2003**, *300*, 1944–1947.
- [48] C. Bressler, M. Chergui, *Chem. Rev.* **2004**, *104*, 1781–1812.
- [49] L. X. Chen, *Angew. Chem.* **2004**, *116*, 2946–2966; *Angew. Chem. Int. Ed.* **2004**, *43*, 2886–2905.
- [50] C. Bressler, R. Abela, M. Chergui, *Z. Kristallogr.* **2008**, *223*, 307–321, and references therein.
- [51] A. Guinier, *X-ray Diffraction*, Dover, New York, **1963**.
- [52] M. Magini, G. Licheri, G. Paschina, G. Piccaluga, G. Pinna, *X-Ray Diffraction of Ions in Aqueous Solutions Hydration and Complex Formation*, CRC, Boca Raton, **1988**.
- [53] B. E. Warren, *X-ray Diffraction*, Dover, New York, **1969**.
- [54] D. T. Cromer, J. B. Mann, *Acta Crystallogr. Sect. A* **1968**, *24*, 321–324.
- [55] F. Hajdu, *Acta Crystallogr. Sect. A* **1972**, *28*, 250–252.
- [56] G. Pálinkás, *Acta Crystallogr. Sect. A* **1973**, *29*, 10–12.
- [57] Gaussian 03, M. J. Frisch, G. W. Trucks, H. B. Schlegel, G. E. Scuseria, M. A. Robb, J. R. Cheeseman, J. A. Montgomery, T. Vreven, K. N. Kudin, J. C. Burant, J. M. Millam, S. S. Iyengar, J. Tomasi, V. Barone, B. Mennucci, M. Cossi, G. Scalmani, N. Rega, G. A. Petersson, H. Nakatsuji, M. Hada, M. Ehara, K. Toyota, R. Fukuda, J. Hasegawa, M. Ishida, T. Nakajima, Y. Honda, O. Kitao, H. Nakai, M. Klene, X. Li, J. E. Knox, H. P. Hratchian, J. B. Cross, V. Bakken, C. Adamo, J. Jaramillo, R. Gomperts, R. E.

- Stratmann, O. Yazyev, A. J. Austin, R. Cammi, C. Pomelli, J. W. Ochterski, P. Y. Ayala, K. Morokuma, G. A. Voth, P. Salvador, J. J. Dannenberg, V. G. Zakrzewski, S. Dapprich, A. D. Daniels, M. C. Strain, O. Farkas, D. K. Malick, A. D. Rabuck, K. Raghavachari, J. B. Foresman, J. V. Ortiz, Q. Cui, A. G. Baboul, S. Clifford, J. Cioslowski, B. B. Stefanov, G. Liu, A. Liashenko, P. Piskorz, I. Komaromi, R. L. Martin, D. J. Fox, T. Keith, M. A. Al-Laham, C. Y. Peng, A. Nanayakkara, M. Challacombe, P. M. W. Gill, B. Johnson, W. Chen, M. W. Wong, C. Gonzalez, J. A. Pople, Gaussian, Inc., Wallingford, CT, **2004**.
- [58] E. Cancès, B. Mennucci, J. Tomasi, *J. Chem. Phys.* **1997**, *107*, 3032–3041.
- [59] K. Refson, *Comput. Phys. Commun.* **2000**, *126*, 310–329.
- [60] R. Longaker, M. M. Litvak, *J. Appl. Phys.* **1969**, *40*, 4033–4041.
- [61] M. Dantus, R. M. Bowman, M. Gruebele, A. H. Zewail, *J. Chem. Phys.* **1989**, *91*, 7437–7450.
- [62] D. P. Zhong, A. H. Zewail, *J. Phys. Chem. A* **1998**, *102*, 4031–4058.
- [63] N. Pugliano, A. Z. Szarka, S. Gnanakaran, M. Triechel, R. M. Hochstrasser, *J. Chem. Phys.* **1995**, *103*, 6498–6511.
- [64] N. Pugliano, A. Z. Szarka, R. M. Hochstrasser, *J. Chem. Phys.* **1996**, *104*, 5062–5079.
- [65] M. Volk, S. Gnanakaran, E. Gooding, Y. Kholodenko, N. Pugliano, R. M. Hochstrasser, *J. Phys. Chem. A* **1997**, *101*, 638–643.
- [66] The values for rate coefficients and time constants are corrected by a factor of 2 with respect to the published values due to a simple error of doubling the rate constant in the global-fitting program for TRXL data.
- [67] J. Fossey, D. Lefort, J. Sorba, *Free Radicals in Organic Chemistry*, Wiley, New York, **1995**.
- [68] H. Ihee, J. Kua, W. A. Goddard, A. H. Zewail, *J. Phys. Chem. A* **2001**, *105*, 3623–3632.
- [69] H. Ihee, A. H. Zewail, W. A. Goddard, *J. Phys. Chem. A* **1999**, *103*, 6638–6649.
- [70] P. S. Skell, D. L. Tuleen, P. D. Readio, *J. Am. Chem. Soc.* **1963**, *85*, 2849–2850.
- [71] Y. L. Li, D. M. Chen, D. Q. Wang, D. L. Phillips, *J. Org. Chem.* **2002**, *67*, 4228–4235.
- [72] X. M. Zheng, D. L. Phillips, *Chem. Phys. Lett.* **2000**, *324*, 175–182.
- [73] D. L. Phillips, W. H. Fang, X. Zheng, Y. L. Li, D. Wang, W. M. Kwok, *Curr. Org. Chem.* **2004**, *8*, 739–755.
- [74] H. Zhang, A. S. Dvornikov, P. M. Rentzepis, *J. Phys. Chem. A* **2005**, *109*, 5984–5988.
- [75] D. A. Oulianov, I. V. Tornov, A. S. Dvornikov, P. M. Rentzepis, *Proc. Natl. Acad. Sci. USA* **2002**, *99*, 12556–12561.
- [76] X. M. Zheng, W. H. Fang, D. L. Phillips, *J. Chem. Phys.* **2000**, *113*, 10934–10946.
- [77] J. G. Bentsen, M. S. Wrighton, *J. Am. Chem. Soc.* **1987**, *109*, 4530–4544.
- [78] B. F. G. Johnson, J. Lewis, M. V. Twigg, *J. Organomet. Chem.* **1974**, *67*, C75–C76.
- [79] J. G. Bentsen, M. S. Wrighton, *J. Am. Chem. Soc.* **1987**, *109*, 4518–4530.
- [80] M. F. Desrosiers, P. C. Ford, *Organometallics* **1982**, *1*, 1715–1716.
- [81] J. Malito, S. Markiewicz, A. Poe, *Inorg. Chem.* **1982**, *21*, 4335–4337.
- [82] J. L. Graff, R. D. Sanner, M. S. Wrighton, *J. Am. Chem. Soc.* **1979**, *101*, 273–275.
- [83] F. W. Grevels, J. G. A. Reuvers, J. Takats, *J. Am. Chem. Soc.* **1981**, *103*, 4069–4073.
- [84] M. F. Desrosiers, D. A. Wink, R. Trautman, A. E. Friedman, P. C. Ford, *J. Am. Chem. Soc.* **1986**, *108*, 1917–1927.
- [85] F. W. Grevels, W. E. Klotzbucher, J. Schrickel, K. Schaffner, *J. Am. Chem. Soc.* **1994**, *116*, 6229–6237.
- [86] E. A. Glascoe, M. F. Kling, J. E. Shanoski, C. B. Harris, *Organometallics* **2006**, *25*, 775–784.
- [87] C. M. Che, L. G. Butler, H. B. Gray, *J. Am. Chem. Soc.* **1981**, *103*, 7796–7797.
- [88] A. E. Stiegman, S. F. Rice, H. B. Gray, V. M. Miskowski, *Inorg. Chem.* **1987**, *26*, 1112–1116.
- [89] D. J. Thiel, P. Livins, E. A. Stern, A. Lewis, *Nature* **1993**, *362*, 40–43.
- [90] P. Coppens, *Chem. Commun.* **2003**, 1317–1320.
- [91] R. M. van der Veen, C. J. Milne, A. E. Nahhas, F. A. Lima, V. T. Pham, J. Best, J. A. Weinstein, C. N. Borca, R. Abela, C. Bressler, M. Chergui, *Angew. Chem.* **2009**, *121*, 2749–2752; *Angew. Chem. Int. Ed.* **2009**, *48*, 2711–2714.
- [92] G. V. Hartland, *Annu. Rev. Phys. Chem.* **2006**, *57*, 403–430.
- [93] M. Perner, S. Gresillon, J. Marz, G. von Plessen, J. Feldmann, J. Porstendorfer, K. J. Berg, G. Berg, *Phys. Rev. Lett.* **2000**, *85*, 792–795.
- [94] C. Burda, X. B. Chen, R. Narayanan, M. A. El-Sayed, *Chem. Rev.* **2005**, *105*, 1025–1102.
- [95] M. Hu, G. V. Hartland, *J. Phys. Chem. B* **2002**, *106*, 7029–7033.
- [96] A. Plech, V. Kotaidis, S. Gresillon, C. Dahmen, G. von Plessen, *Phys. Rev. B* **2004**, *70*, 195423.
- [97] A. Plech, S. Kurbitz, K. J. Berg, H. Graener, G. Berg, S. Gresillon, M. Kaempfe, J. Feldmann, M. Wulff, G. von Plessen, *Europhys. Lett.* **2003**, *61*, 762–768.
- [98] V. Kotaidis, C. Dahmen, G. von Plessen, F. Springer, A. Plech, *J. Chem. Phys.* **2006**, *124*, 184702.
- [99] V. Kotaidis, A. Plech, *Appl. Phys. Lett.* **2005**, *87*, 213102.
- [100] A. Plech, V. Kotaidis, M. Lorenc, M. Wulff, *Chem. Phys. Lett.* **2005**, *401*, 565–569.
- [101] M. Cammarata, M. Levantino, F. Schotte, P. A. Anfinrud, F. Ewald, J. Choi, A. Cupane, M. Wulff, H. Ihee, *Nat. Methods* **2008**, *5*, 881–887.
- [102] E. T. J. Nibbering, H. Fidder, E. Pines, *Annu. Rev. Phys. Chem.* **2005**, *56*, 337–367.
- [103] P. Kukura, D. W. McCamant, R. A. Mathies, *Annu. Rev. Phys. Chem.* **2007**, *58*, 461–488.
- [104] P. Hamm, M. H. Lim, R. M. Hochstrasser, *J. Phys. Chem. B* **1998**, *102*, 6123–6138.
- [105] J. Zheng, K. Kwak, M. D. Fayer, *Acc. Chem. Res.* **2007**, *40*, 75–83.
- [106] L. X. Chen, X. Y. Zhang, E. C. Wasinger, K. Attenkofer, G. Jennings, A. Z. Muresan, J. S. Lindsey, *J. Am. Chem. Soc.* **2007**, *129*, 9616–9618.
- [107] W. Gawelda, V. T. Pham, M. Benfatto, Y. Zaushitsyn, M. Kaiser, D. Grolimund, S. L. Johnson, R. Abela, A. Hauser, C. Bressler, M. Chergui, *Phys. Rev. Lett.* **2007**, *98*, 057401.
- [108] W. Gawelda, M. Johnson, F. M. F. de Groot, R. Abela, C. Bressler, M. Chergui, *J. Am. Chem. Soc.* **2006**, *128*, 5001–5009.
- [109] V. T. Pham, W. Gawelda, Y. Zaushitsyn, M. Kaiser, D. Grolimund, S. L. Johnson, R. Abela, C. Bressler, M. Chergui, *J. Am. Chem. Soc.* **2007**, *129*, 1530–1531.
- [110] L. X. Chen, W. J. H. Jager, G. Jennings, D. J. Gosztola, A. Munkholm, J. P. Hessler, *Science* **2001**, *292*, 262–264.

Received: February 28, 2009

Published online on July 7, 2009